Research Square

Preprints are preliminary reports that have not undergone peer review.
They should not be considered conclusive, used to inform clinical practice,
or referenced by the media as validated information.

Neural dynamics of temporal-order errors despite preserved identity in rapid visual sequences

Zong Meng
Beijing Normal University https://orcid.org/0000-0002-8701-9366
Qi Chen
Beijing Normal University
Liqin Zhou
Beijing Normal University
Ke Zhou
Beijing Normal University
Antao Chen
antao.chen@sjtu.edu.cn

Shanghai Jiao Tong University

Research Article

Keywords:

Posted Date: November 18th, 2026

DOI: https://doi.org/10.21203/rs.3.rs-11765230/v1

License: This work is licensed under a Creative Commons Attribution 4.0 International License.
Read Full License

Additional Declarations: The authors declare no competing interests.

Neural dynamics of temporal-order errors despite preserved identity in rapid visual sequences

Zong Meng[1, 2], Qi Chen [3], Liqin Zhou [3], Ke Zhou [3], and Antao Chen [4*]

[1] State Key Laboratory of Cognitive Neuroscience and Learning & IDG/McGovern Institute for Brain Research, Beijing Normal University, Beijing 100875, China

[2] Key Laboratory of Cognition and Personality of Ministry of Education, Faculty of Psychology, Southwest University, Chongqing 400715, China

[3] Beijing Key Laboratory of Applied Experimental Psychology, National Demonstration Center for Experimental Psychology Education (Beijing Normal University), Faculty of Psychology, Beijing Normal University, Beijing 100875, China

[4] Brain Health Institute, National Center for Mental Disorders, Shanghai Mental Health Center, Shanghai Jiao Tong University School of Medicine and School of Psychology, Shanghai 200030, China

Address correspondence to Antao Chen, Shanghai Jiao Tong University School of Medicine and School of Psychology, No. 1954, Huashan Road, Xuhui District, Shanghai 200030, China

Email: antao.chen@sjtu.edu.cn

Abstract

Preserving the order of visual events is fundamental to understanding a rapidly changing environment, yet successful identification does not guarantee accurate order reporting. We recorded electroencephalography from 27 adults during rapid serial visual presentation, comparing correct- and reversed-order reports when both target identities were correctly reported. N2pc, P3b, pretarget phase, and phase–amplitude coupling measures did not support the tested theoretical predictions. Correct-order trials showed a more negative posterior event-related potential around 400 ms after the first target, with source estimates implicating right posterior cortex. Its amplitude was associated with single-trial outcomes, and control comparisons suggested that target load or identity-report success alone did not explain the effect. This posterior involvement extended to oscillatory activity, with greater right posterior beta power around target onset and greater beta and theta–alpha power later. These changes were accompanied by stronger post-target low-frequency phase consistency across trials and enhanced late frontal–right-occipital synchronization. Together, these findings advance understanding of rapid visual “when” processing by linking the preservation of event order to later right posterior activity and frontal–occipital coordination.

Introduction

Adaptive behavior in a changing visual environment requires knowing what happened, where it happened, and how events unfolded over time. The same events can convey different information when their order changes, making temporal order an essential part of the visual “when” dimension (e.g., refs. [1,2]). Representing a sequence therefore requires both identifying its constituent events and preserving their relative temporal positions. This becomes particularly challenging when events occur in rapid succession: their neural responses overlap, yet the events must remain distinguishable within the emerging sequence. How does the brain preserve this temporal structure, and why can order be lost even when the events themselves remain accurately reportable?

Lag-1 order reversals in rapid serial visual presentation (RSVP) provide an informative setting for investigating this problem. In RSVP, observers report targets embedded within rapidly presented distractor streams. When a second target (T2) immediately follows the first (T1), observers can correctly report both target identities while reversing their temporal order (e.g., refs. [3–5]). Comparing correct and reversed reports therefore allows order accuracy to be examined when identity report is successful, providing a tractable approach to studying the temporal organization of rapidly successive events.

The prior-entry account proposes that attentional enhancement triggered by T1 can favor the immediately following T2, allowing T2 to enter working

63 memory first despite its later onset (e.g., refs. [6,7]). Consistent with this account,
64 cueing T1 reduces order reversals, whereas cueing T2 increases them (e.g.,
65 ref. [8]). A delayed-engagement implementation predicts later onset of the N2
66 posterior contralateral (N2pc) component of the event-related potential (ERP)
67 on reversed-order than on correct-order trials, reflecting delayed attentional
68 engagement (e.g., refs. [9,10]). The temporal integration account instead
69 proposes that adjacent targets can share an event representation, preserving
70 their identities while weakening the distinction between their temporal
71 positions (e.g., refs. [4,11,12]). Behavioral support comes from reports of single
72 composite percepts formed from consecutive targets (e.g., ref. [13]) and from
73 greater reversal rates for same-category than different-category targets [14],
74 suggesting that representational relationships between targets may modulate
75 integration and order reporting. If reversals involve encoding the two targets
76 within one event with reduced consolidation demands, they should elicit
77 smaller P3b amplitudes than correct-order reports, by analogy with the
78 smaller P3b responses to explicitly integrated percepts than to separately
79 reported targets [15]. The categorical-similarity finding further motivates
80 exploring whether reversal probability varies with numerical proximity within
81 the digit category. However, it remains unclear whether these ERP measures
82 are associated with temporal-order accuracy when both target identities are
83 correctly reported.

84 Evidence from related areas of temporal perception and sequence

memory suggests additional neural processes relevant to order reporting. First, lesion and transcranial magnetic stimulation (TMS) studies implicate right posterior regions in visual temporal-order judgments, providing evidence for hemispheric asymmetries in the processing of visual event timing (e.g., refs. [16–18]). These findings motivate examining posterior activity and exploring whether order accuracy varies with target visual field. Second, oscillatory power and phase may reflect variations in cortical excitability and rhythmic information sampling, helping characterize the neural states in which continuous input is processed and organized (e.g., refs. [19–21]). Studies of visual detection have associated prestimulus low-frequency phase with whether a subsequent target is detected (e.g., refs. [22,23]). More directly related to order perception, parieto-occipital alpha phase before and around the first stimulus differs between correct and reversed tactile order judgments when the arms are crossed [24]. Third, cross-frequency phase–amplitude coupling (PAC) may contribute to sequential organization by coordinating high-frequency activity relative to low-frequency phase (e.g., refs. [25,26]). Theta–gamma coupling strength has been associated with ordering demands and performance on tasks involving the ordering of information (e.g., refs. [27,28]). These findings identify candidate neural states and forms of temporal coordination, but their relationship to correct versus reversed reports of rapid, same-location visual events, when both identities are correctly reported, remains to be established.

Here, we recorded electroencephalography (EEG) during a bilateral RSVP task in which participants reported colored digit targets embedded in distractor streams. On dual-target trials, T1 and T2 appeared consecutively at the same location with a 100-ms stimulus-onset asynchrony. Intermixed single-target trials included a condition in which a colored target was followed by a gray digit distractor, enabling complementary examination of target–distractor order reports. Our central comparison contrasted correct-order (CO) and order-reversal (OR) trials in which both target identities were correctly reported, examining order outcomes under successful identity report and without a spatial shift between targets. We tested the specific predictions of the prior-entry and temporal integration accounts using N2pc onset latency and P3b amplitude, respectively. We further assessed whether candidate neural correlates suggested by related fields—posterior ERP activity, oscillatory power and phase, and PAC strength—distinguished order outcomes, and explored interregional coordination. Guided by the categorical-similarity findings and evidence of lateralized visual processing, we also explored whether reversal probability varied with numerical distance and target visual field. The tested predictions concerning N2pc, P3b, pretarget phase, and PAC were not reliably supported. Accurate order reports were associated with a late posterior ERP response, right posterior power dynamics, and frontal–right-occipital coordination. These findings link the temporal organization of rapidly presented visual events to posterior

processing and its coordination with frontal systems.

Results

Behavioral characteristics of temporal-order reversals

Participants reported T2 before T1 on an average of 12.56% of all dual-target (TT) trials (*SD* = 8.69%), significantly exceeding the chance probability expected under the task constraints (mean difference = 10.77 %, 95% CI [7.33, 14.21]; $t(26) = 6.44$, $p < 0.001$, $d = 1.24$; **Fig. 1c**). Because participants were informed that the two targets were always different, chance corresponded to randomly selecting the two target identities from eight possible digits and reporting them in reversed order: 1/(8 × 7) = 1.79%. Reversal rates also exceeded the rates of partial reports in which only T1 was correctly identified (*M* = 6.23%, *SD* = 4.93%; $p_{Holm} = 0.017$) or only T2 was correctly identified (*M* = 3.56%, *SD* = 3.06%; $p_{Holm} < 0.001$; **Supplementary Fig. 1a**). Thus, temporal-order reversals were a systematic feature of performance rather than an outcome of guessing.

Previous studies have reported visual-field asymmetries in temporal judgments (e.g., refs. [29–31]) and shown that categorical similarity and numerical ordinality can influence order reports [14,32]. Building on these findings, we explored whether reversal probability varied with target visual field and numerical distance. Reversal rates were higher for targets presented

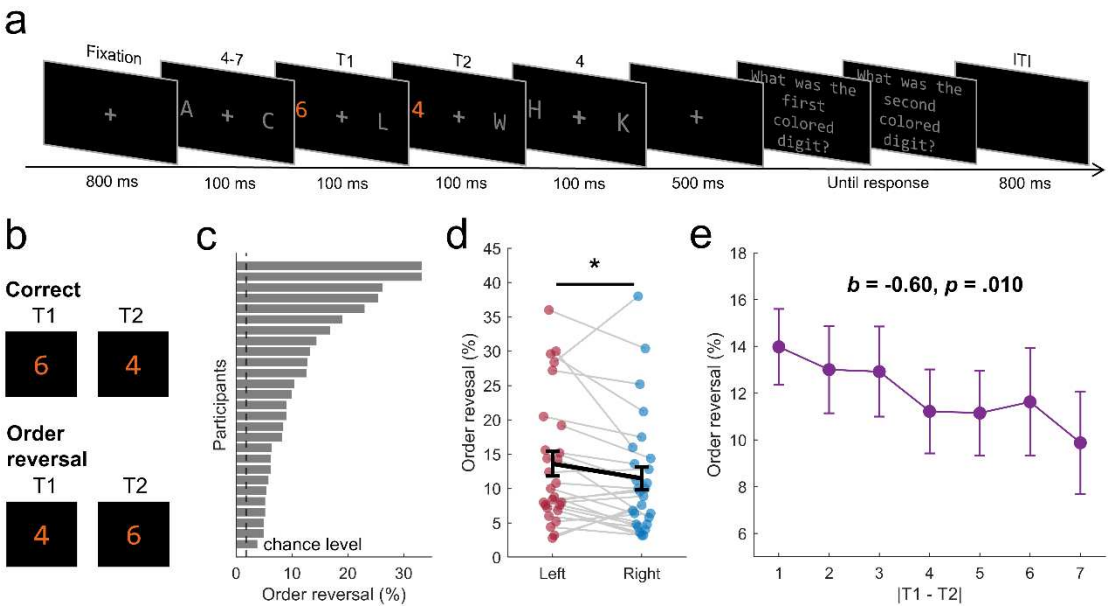
in the left visual field (M = 13.61%, SD = 9.30%) than in the right visual field (M = 11.50%, SD = 8.65%; $t(26) = 2.41$, $p = 0.023$, $d = 0.46$, 95% CI [0.31%, 3.91%]; **Fig. 1d**). To characterize the numerical relationship, we decomposed the signed difference between the targets into numerical distance (|T1 − T2|; 1–7) and numerical direction (T1 > T2 vs. T1 < T2). A repeated-measures analysis of variance (ANOVA) revealed a main effect of numerical distance ($F(6, 156) = 3.70$, $p = 0.002$, $\omega^2 = 0.018$). Reversal rates decreased with increasing numerical distance, with a mean participant-level slope of −0.60 percentage points per unit increase in distance ($b = -0.60$, $SE = 0.22$, $t(26) = -2.79$, $p = 0.010$; **Fig. 1e**). Neither numerical direction ($F(1, 26) = 0.73$, $p = 0.402$, $\omega^2 < 0.001$) nor its interaction with distance ($F(6, 156) = 0.40$, $p = 0.880$, $\omega^2 < 0.001$) was significant. Among trials in which both target identities were correctly reported, separate single-trial generalized linear mixed-effects models (GLMMs) showed that larger numerical distances were associated with lower reversal probabilities ($b = -0.15$, $SE = 0.03$, $z = -5.02$, $p < 0.001$), whereas left-field presentation was associated with higher reversal probabilities (b = -0.20, SE = 0.06, z = -3.55, p = 0.004). Thus, order reversals were more likely for numerically proximal targets and for targets presented in the left visual field.

We also compared the proportion of fully correct reports across T, TT, and TD trials (see **Supplementary Fig. 1c** for details). Accuracy required a correct target report followed by a correct indication that no second target was

present in T and TD trials, and correct reports of both target identities in presentation order in TT trials. A repeated-measures ANOVA revealed a main effect of trial type ($F(1.51, 39.29) = 61.02$, $p < 0.001$, $\omega^2 = 0.49$). Post hoc comparisons confirmed that accuracy was higher in T ($M = 93.12\%$, $SD = 6.41\%$) than in both TT ($M = 69.60\%$, $SD = 16.41\%$; $p_{Holm} < 0.001$) and TD ($M = 53.20\%$, $SD = 22.97\%$; $p_{Holm} < 0.001$), and higher in TT than in TD ($p_{Holm} = 0.001$).

We examined distractor-intrusion (DI) patterns in TD trials [10,33]. In addition to trials in which only the distractor was reported (DI_D; $M = 7.58\%$, $SD = 6.22\%$), participants frequently reported the distractor alongside the target, yielding intrusions in which the target and distractor were reported in their presented order (DI_TD; $M = 28.08\%$, $SD = 19.03\%$) or in reversed order (DI_DT; $M = 7.06\%$, $SD = 7.98\%$; **Supplementary Fig. 1d**). We then examined whether individual differences in these intrusion patterns were associated with dual-target reversal rates. Across participants, the dual-target reversal rate was strongly correlated with DI_DT ($r = 0.87$, $p < 0.001$; **Supplementary Fig. 1e**), but not with DI_TD ($r = 0.17$, $p = 0.398$) or DI_D ($r = 0.29$, $p = 0.146$; **Supplementary Fig. 1f**). The association with DI_DT remained significant after controlling for accuracy across all three trial types ($r_{partial} = 0.73$, $p < 0.001$), whereas the corresponding partial correlations with DI_TD ($r_{partial} = -0.30$, $p = 0.148$) and DI_D ($r_{partial} = -0.17$, $p = 0.427$) were not significant. Moreover, the correlation with DI_DT was stronger than those with

DI_TD (Steiger's z = 4.44, p < 0.001) and DI_D (Steiger's z = 3.60, p < 0.001). This selective association is consistent with a shared tendency toward reversed-order reporting across TT and TD trials.



N2pc and P3b measures do not reliably distinguish report order

We next compared N2pc and P3b responses between CO and OR trials to assess ERP correlates of attentional selection and postperceptual target encoding, respectively. We found no reliable difference in N2pc mean amplitude between CO and OR trials (CO: M = −3.38, SD = 1.89 μV; OR: M = −3.28, SD = 2.28 μV; t(26) = −0.57, p = 0.572, 95% CI [−0.47, 0.26], d = −0.11; **Fig. 2a**), and a Bayesian paired t-test provided moderate evidence for the null (BF_{01} = 4.22). The 25% fractional-area latency of the N2pc also showed no significant difference between CO (M = 214.71 ms) and OR trials (M = 217.04 ms; t_{adj}(26) = −0.91, p = 0.369; **Fig. 2a**). Similarly, the P3b amplitude did not reliably differ between CO (M = 3.33, SD = 2.07 μV) and OR trials (M = 3.17,

SD = 2.18 μV; $t(26) = 1.14$, $p = 0.263$, 95% CI [−0.13, 0.45], $d = 0.22$; **Fig. 2b**), with the Bayesian evidence weakly favoring the null ($BF_{01} = 2.72$). Cluster-based permutation tests of ERP time courses from the N2pc and P3b electrode sets revealed no significant clusters differentiating CO and OR trials.

At the single-trial level, logistic GLMMs tested whether N2pc or P3b amplitude was associated with report outcome. Neither N2pc amplitude ($b = 0.02$, $SE = 0.03$, $z = 0.64$, $p = 0.524$; **Supplementary Fig. 2a**) nor P3b amplitude ($b = 0.02$, $SE = 0.03$, $z = 0.48$, $p = 0.632$; **Supplementary Fig. 2b**) showed a significant association with reversal probability. We additionally explored whether these amplitude–outcome associations varied with numerical distance or target visual field. None of the interactions reached significance (N2pc × numerical distance: $b = 0.01$, $SE = 0.03$, $z = 0.34$, $p = 0.734$, **Supplementary Fig. 2g**; N2pc × visual field: $b = -0.05$, $SE = 0.06$, $z = -0.84$, $p = 0.400$, **Supplementary Fig. 2d**; P3b × numerical distance: $b = -0.03$, $SE = 0.03$, $z = -1.11$, $p = 0.265$, **Supplementary Fig. 2h**; P3b × visual field: $b = 0.03$, $SE = 0.06$, $z = 0.51$, $p = 0.610$, **Supplementary Fig. 2e**).

Together, CO and OR trials did not differ reliably in N2pc onset latency or amplitude or in P3b amplitude, and single-trial N2pc and P3b amplitudes were not reliably associated with reversal probability. These findings did not support the specific predictions tested here: delayed N2pc onset derived from the prior-entry account and reduced P3b amplitude derived from the temporal integration account.

A late posterior negativity distinguishes correct-order from reversed-order reports

An exploratory cluster-based permutation analysis of posterior ERP activity identified a negative CO–OR cluster spanning approximately 392–476 ms after T1 onset (t_{sum} = −63.70, $p_{cluster}$ = 0.003; **Fig. 2c**). For descriptive purposes, we refer to this effect as the occipital N400 (ON400). Mean amplitude within this interval was more negative for CO (*M* = −0.03, *SD* = 2.66 μV) than for OR trials (*M* = 0.70, *SD* = 2.70 μV; *t*(26) = −3.92, *p* < 0.001, 95% CI [−1.11, −0.35], *d* = −0.76; **Fig. 2d**). A follow-up spatial cluster-based permutation analysis identified a cluster spanning occipital and parietal electrodes (Oz, O1, O2, PO3, PO5–PO8, P3, P5 and P7; t_{sum} = −33.73, $p_{cluster}$ = 0.012; **Fig. 2c**).

We used standardized low-resolution brain electromagnetic tomography (sLORETA) to estimate the cortical distribution of the CO–OR difference within the ON400 time window. Source-space cluster-based permutation testing identified a significant CO–OR cluster (t_{sum} = −3375.66, $p_{cluster}$ = 0.010). The estimated source distribution extended across right posterior visual and association cortices, including occipital, inferior parietal, temporoparieto-occipital, and lateral temporal regions (**Fig. 2e**).

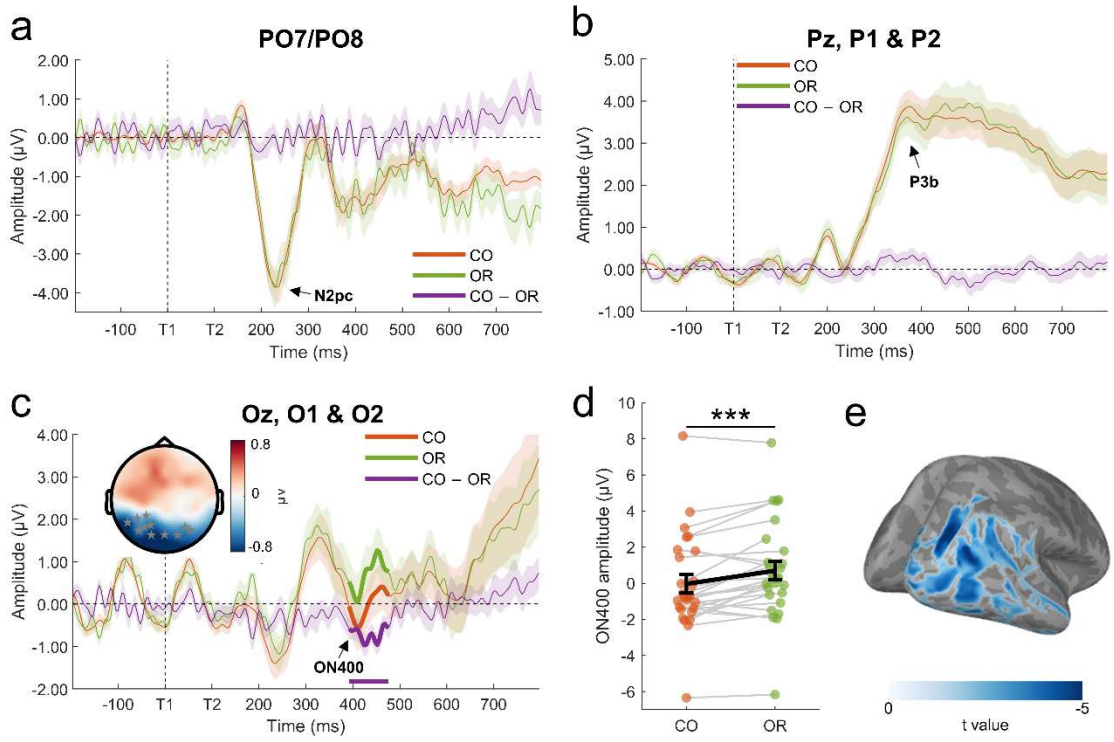
We next examined the association between ON400 amplitude and report outcome at the single-trial level using a logistic GLMM. ON400 amplitude was significantly associated with reversal probability (*b* = 0.14, *SE* = 0.03, *z* = 4.42,

$p < 0.001$; **Supplementary Fig. 2c**): more positive ON400 amplitudes were associated with a higher probability of order reversal. We further explored whether this association varied with target visual field or numerical distance. Neither the ON400 × visual-field interaction ($b = -0.003$, $SE = 0.058$, $z = -0.04$, $p = 0.964$; **Supplementary Fig. 2f**) nor the ON400 × numerical-distance interaction ($b = -0.003$, $SE = 0.030$, $z = -0.10$, $p = 0.917$; **Supplementary Fig. 2i**) was significant. Thus, the association between ON400 amplitude and report outcome did not reliably vary with target location or numerical distance.

To further assess whether the ON400 was specifically associated with report order, we first compared DI_TD and DI_DT trials within the TD condition. We then conducted two additional comparisons to examine possible contributions of target load and target-identification success. All mean-amplitude comparisons used the time window and electrode set defined exclusively by the CO–OR contrast in TT trials. For comparisons involving less frequent response categories, eligibility was determined separately for each comparison: participants were excluded if they contributed fewer than 15 artifact-free trials to either condition. Among the 18 eligible participants, mean amplitudes were more negative for DI_TD trials ($M = -0.28$, $SD = 2.55$ μV) than for DI_DT trials ($M = 0.50$, $SD = 3.07$ μV; $t(17) = -2.86$, $p = 0.011$, 95% CI [−1.36, −0.20]**,** $d = -0.67$; **Supplementary Fig. 3a**). A complementary cluster-based permutation analysis identified an occipital DI_TD–DI_DT

difference spanning 404–444 ms after target onset (t_{sum} = −27.41, $p_{cluster}$ = 0.019; **Supplementary Fig. 3a**). To assess the contribution of target load, we compared correct T trials with CO trials. This comparison included all 27 participants and revealed no significant difference ($t(26)$ = −0.73, p = 0.471, 95% CI [−0.67, 0.32], d = −0.14, BF_{01} = 3.84; **Supplementary Fig. 3b**). To assess the contribution of target-identification success, we compared CO trials with TT trials in which only one target identity was correctly reported. This comparison included 25 eligible participants and likewise revealed no significant difference ($t(24)$ = −1.36, p = 0.186, 95% CI [−0.65, 0.13], d = −0.27, BF_{01} = 2.09; **Supplementary Fig. 3c**).

Together, these findings link the ON400 to accurate temporal-order reporting, with source estimates pointing to right posterior cortical regions and single-trial analyses showing that more negative amplitudes were associated with a lower probability of reversal. Control comparisons within the selected ON400 window suggest that the mean-amplitude effect is not readily explained solely by target load or identity-report success.



291

292

293 **Right posterior power dynamics are associated with report order**

294 We compared time–frequency power between CO and OR trials across
295 predefined regions of interest (ROIs), with a particular focus on the right
296 posterior ROI. This focus was motivated by prior lesion and TMS evidence
297 implicating right posterior regions in visual temporal-order judgments (e.g.,
298 refs. [16–18]) and by the right posterior source distribution of the ON400
299 difference. The analysis identified two significant power clusters, both within
300 the right posterior ROI. No significant clusters were observed in the remaining
301 ROIs (see **Supplementary Fig. 4** for details). Complementary analyses of
302 contralateral-minus-ipsilateral power in anterior, central, and posterior lateral
303 ROIs likewise revealed no significant clusters (**Supplementary Fig. 4**).

The first cluster comprised an early peri-target beta effect spanning approximately 11–20 Hz and −150 to 200 ms relative to T1 onset (t_{sum} = 1667.21, $p_{cluster}$ = 0.021; **Fig. 3a**). A follow-up spatial cluster-based permutation analysis identified a cluster over right posterior parietal and frontocentral electrodes (t_{sum} = 45.13, $p_{cluster}$ = 0.004; **Fig. 3b**). Mean beta power was higher for CO (M = −0.79, SD = 0.80 dB) than for OR trials (M = −1.13, SD = 0.88 dB; $t(26) = 4.10$, $p < 0.001$, d = 0.79, 95% CI [0.17, 0.52]; **Fig. 3b**).

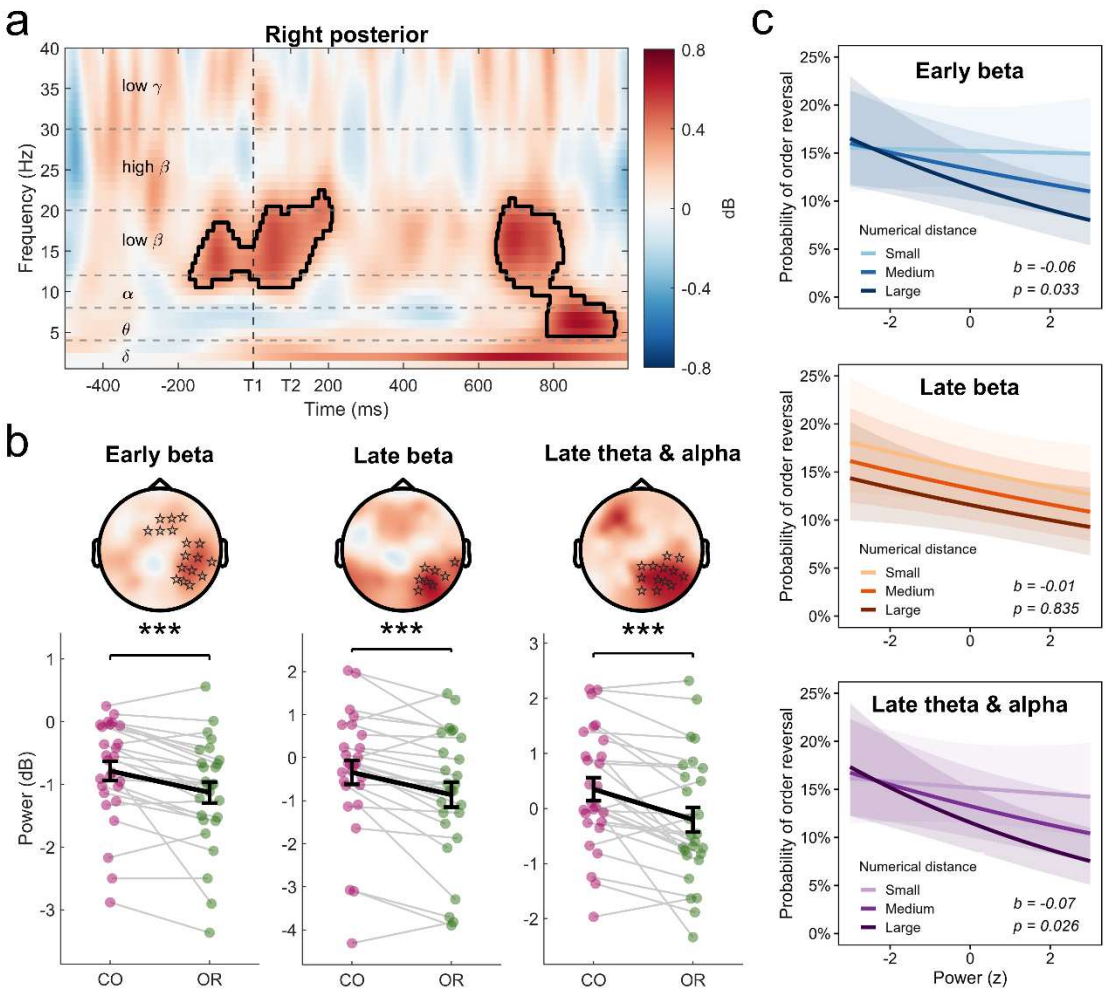
The second cluster spanned approximately 5–20 Hz and 650–960 ms after T1 onset (t_{sum} = 1695.22, $p_{cluster}$ = 0.020). For descriptive purposes, we divided this cluster into a late beta portion (approximately 650–800 ms) and a subsequent theta–alpha portion (approximately 800–960 ms). The late beta effect was distributed mainly over right lateral occipitotemporal electrodes (t_{sum} = 28.69, $p_{cluster}$ = 0.029), with higher power for CO (M = −0.34, SD = 1.43 dB) than for OR trials (M = −0.86, SD = 1.50 dB; $t(26) = 4.34$, $p < 0.001$, 95% CI [0.27, 0.77], d = 0.84; **Fig. 3b**). The subsequent theta–alpha effect extended over right occipital, parietal, and temporal electrodes (t_{sum} = 37.38, $p_{cluster}$ = 0.005), again with higher power for CO (M = 0.14, SD = 0.98 dB) than for OR trials (M = −0.36, SD = 1.11 dB; $t(26) = 4.21$, $p < 0.001$, d = 0.81, 95% CI [0.25, 0.74]; **Fig. 3b**).

Separate logistic GLMMs tested whether each power measure was associated with report outcome at the single-trial level, with a participant-

specific random intercept. Higher power was associated with a lower probability of order reversal for all three measures: early beta (b = −0.08, SE = 0.03, z = −2.61, p = 0.009; **Supplementary Fig. 5a**), late beta (b = −0.08, SE = 0.03, z = −2.70, p = 0.007; **Supplementary Fig. 5b**), and late theta–alpha power (b = −0.09, SE = 0.03, z = −2.89, p = 0.004; **Supplementary Fig. 5c**). Thus, stronger power in each feature was associated with a greater likelihood of correct-order reporting.

We further examined whether the associations between single-trial power and report outcome varied with target visual field or numerical distance by adding the corresponding interaction terms to separate GLMMs. None of the power × visual field interactions was significant (early beta: b = 0.002, SE = 0.06, z = 0.04, p = 0.968; late beta: b = 0.007, SE = 0.06, z = 0.12, p = 0.908; late theta–alpha: b = −0.060, SE = 0.06, z = −1.03, p = 0.302; **Supplementary Fig. 5d–f**). The power × numerical distance interactions reached significance for early beta (b = −0.06, SE = 0.03, z = −2.13, p = 0.033; **Fig. 3c**) and late theta–alpha power (b = −0.07, SE = 0.03, z = −2.22, p = 0.026; **Fig. 3c**). The interaction with late beta power was not significant (b = −0.006, SE = 0.03, z = −0.21, p = 0.835; **Fig. 3c**). Follow-up simple-slope analyses further showed that early beta power did not significantly predict order reversal at small numerical distances (b = −0.008, SE = 0.04, z = −0.19, p_{Holm} = 0.851) but showed significant negative associations at medium (b = −0.07, SE = 0.03, z = −2.33, p_{Holm} = 0.040) and large numerical distances (b =

−0.14, SE = 0.05, z = −3.03, p_{Holm} = 0.007). A similar pattern was observed for late theta–alpha power, which was not significantly associated with order reversal at small numerical distances (b = −0.02, SE = 0.04, z = −0.61, p_{Holm} = 0.542), but significantly predicted a lower likelihood of order reversal at medium (b = −0.091, SE = 0.03, z = −3.00, p_{Holm} = 0.005) and large numerical distances (b = −0.16, SE = 0.044, z = −3.55, p_{Holm} = 0.001). These findings indicate that the relationship between early beta and late theta–alpha power and order-reversal probability was modulated by numerical distance, becoming more pronounced when the two target digits were more numerically distinct. In contrast, we found no evidence that the late beta effect varied with numerical distance.



Post-target low-frequency phase consistency but not phase opposition or phase–amplitude coupling, differentiates temporal order reports

We next compared inter-trial phase coherence (ITPC) between CO and OR trials. To account for trial-count bias in ITPC, we matched the number of CO and OR trials within each participant by random subsampling before estimating ITPC. Cluster-based permutation testing identified a significant low-frequency ITPC cluster, with the effect most pronounced at 1–4 Hz approximately 150–850 ms after T1 onset (t_{sum} = 1847.86, $p_{cluster}$ < 0.001; **Fig. 4a**). Mean ITPC averaged across all scalp electrodes over 1–4 Hz and 150–850 ms was higher for CO (*M* = 0.34, *SD* = 0.05) than OR trials (*M* = 0.32, *SD*

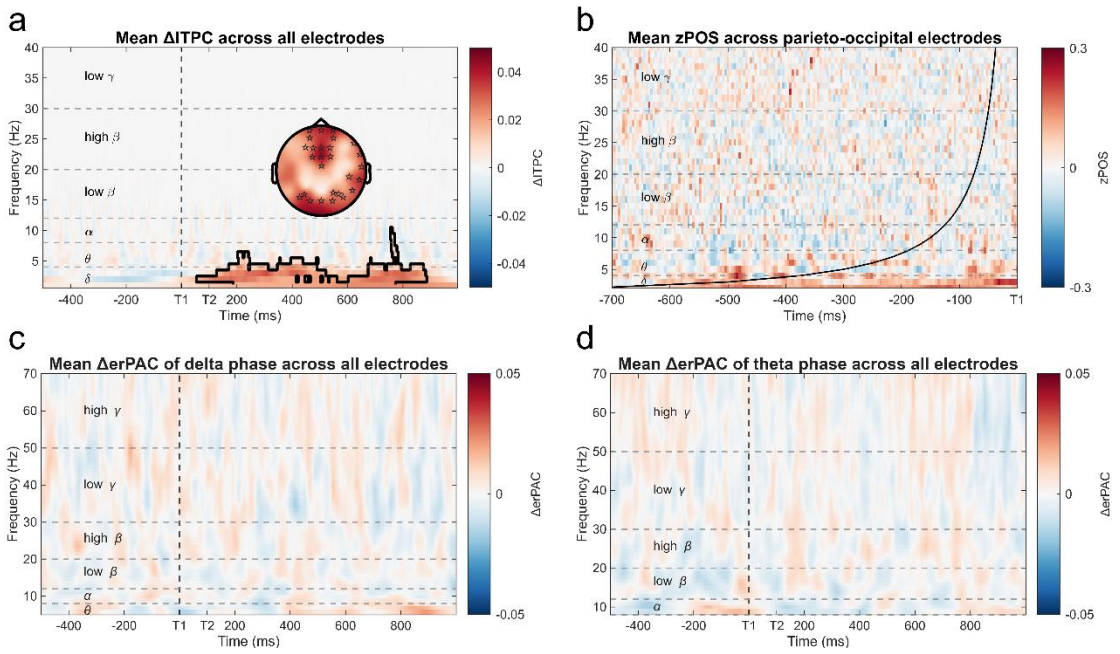
= 0.05; $t(26) = 4.28$, $p < 0.001$, 95% CI [0.01, 0.03], $d = 0.82$; **Supplementary Fig. 6a**). A spatial cluster-based permutation analysis identified a cluster encompassing frontal, bilateral occipital, and right temporoparietal electrodes ($t_{sum} = 87.08$, $p_{cluster} < 0.001$; **Fig. 4a**). To further assess the robustness of this phase-consistency effect, we also computed pairwise phase consistency (PPC), a complementary measure of inter-trial phase consistency that is less sensitive to trial-count differences. The PPC analysis likewise indicated greater low-frequency phase consistency for CO than for OR trials, with a similar time–frequency range and scalp distribution (**Supplementary Fig. 6b–c**). These findings indicate that correct-order reports were associated with greater post-target low-frequency phase consistency across trials.

We next used the phase-opposition sum (POS) to test whether CO and OR trials were associated with distinct preferred phases before T1 onset. We prioritized the parieto-occipital ROI based on previous evidence linking posterior alpha phase to visual detection [23,34] and tactile temporal-order judgments [24]. The analysis was restricted to the pretarget interval, excluding time–frequency points potentially contaminated by temporal smearing of post-target activity. No significant clusters were identified within the parieto-occipital ROI (all cluster-level *p*s > 0.271; **Fig. 4b**). A supplementary analysis averaging electrode-level zPOS across all scalp electrodes likewise revealed no significant clusters (all cluster-level *p*s > 0.232; **Supplementary Fig. 7**). Thus, neither analysis provided reliable evidence that CO and OR trials were

associated with different preferred phases before T1 onset.

Finally, we compared event-related phase–amplitude coupling (erPAC) between CO and OR trials. This measure quantifies the across-trial association between low-frequency phase and higher-frequency amplitude at each time point. Motivated by theta–gamma coding accounts and evidence linking coupling strength to ordering demands and task performance (e.g., refs. [27,28]), we examined coupling between theta phase (4–7 Hz) and amplitude at 8–70 Hz. As an exploratory follow-up to the delta-band ITPC effect reported above, we also examined coupling between delta phase (1–4 Hz) and amplitude at 5–70 Hz. Both analyses used erPAC averaged across all scalp electrodes. Neither analysis identified significant CO–OR clusters within the examined time–frequency range (minimum cluster-level $p = 0.507$ for delta and 1.000 for theta; **Fig. 4c–d**). Thus, we found no reliable evidence that correct and reversed temporal-order reports differed in mean delta- or theta-based erPAC across scalp electrodes.

Together, the ITPC and PPC analyses associated correct-order reports with greater low-frequency phase consistency across trials after target onset. No reliable differences between report outcomes were detected in pretarget phase or erPAC involving delta or theta phase.



411

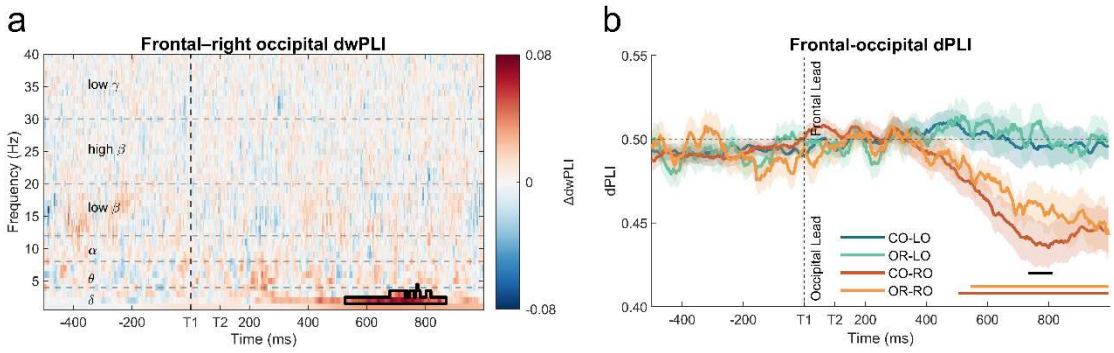
412 **Correct-order reports are associated with stronger late frontal–right-**
413 **occipital connectivity**

414 The ITPC and PPC analyses revealed outcome-related differences in post-
415 target low-frequency phase consistency across trials, with effects involving
416 frontal and bilateral occipital electrodes. To examine whether temporal-order
417 accuracy was also associated with phase synchronization between spatially
418 separated electrode groups, we conducted exploratory functional connectivity
419 (FC) analyses. We assessed frontal–left-occipital and frontal–right-occipital
420 connections separately, guided by the right posterior distribution of the ON400
421 source estimates and oscillatory effects, together with lesion and TMS
422 evidence implicating right posterior cortex in visual temporal-order judgments
423 (e.g., refs. [16–18]). FC was quantified using the debiased weighted phase-lag
424 index (dwPLI), which measures non-zero-lag phase synchronization while
425 reducing sensitivity to volume conduction and finite-sample bias [35].

Comparison of dwPLI between CO and OR trials revealed a significant frontal–right-occipital connectivity cluster spanning approximately 530–860 ms after T1 onset in the 2–3 Hz frequency range (t_{sum} = 370.42, $p_{cluster}$ = 0.016; **Fig. 5a**). Mean dwPLI averaged across frontal–right-occipital electrode pairs over 2–3 Hz and 530–860 ms was higher for CO (M = 0.08, SD = 0.08) than for OR trials (M = 0.04, SD = 0.06; $t(26) = 4.30$, $p < 0.001$, 95% CI [0.02, 0.06], d = 0.83; **Supplementary Fig. 8a**). In contrast, no significant connectivity differences were observed between frontal and left occipital electrodes (all cluster-level ps > 0.264; **Supplementary Fig. 8b**).

To further characterize phase-leading asymmetry within the significant frontal–right-occipital network, we computed the directed phase-lag index (dPLI) [36]. To control for unequal trial counts, we matched CO and OR trial numbers within each participant using random subsampling and averaged condition-specific dPLI estimates across 1,000 iterations. dPLI was below 0.5 within significant late clusters extending from approximately 504 to 996 ms in CO trials (t_{sum} = −505.31, $p_{cluster} < 0.001$) and from 544 to 996 ms in OR trials (t_{sum} = −375.98, $p_{cluster} < 0.001$; **Fig. 5b**). Moreover, the right-occipital lead was significantly stronger for CO than OR trials between approximately 730 and 810 ms (t_{sum} = −52.47, $p_{cluster}$ = 0.041; **Fig. 5b**). For frontal–left-occipital electrode pairs, dPLI did not differ significantly from 0.5 in either condition (all cluster-level ps > 0.135), and no significant difference between CO and OR trials was detected (all cluster-level ps > 0.610; **Fig. 5b**). Together, these

results associate correct temporal-order reports with stronger frontal–right-occipital connectivity and a more consistent late right-occipital phase lead relative to frontal activity.



Discussion

Coherent visual experience requires the brain to preserve the temporal relations among events. We examined the neural dynamics of this process by comparing correct and reversed order reports when both target identities were correctly reported and the targets shared a spatial location. Several predictions motivated by existing accounts and related research were not supported by the measures tested here: CO and OR trials did not reliably differ in N2pc onset latency or amplitude, P3b amplitude, pretarget phase, or delta- and theta-based erPAC. The positive findings identified converging electrophysiological correlates of accurate temporal organization: a more negative ON400, higher right posterior power, more consistent post-target low-frequency phase, and stronger frontal–right-occipital synchronization. Later right posterior activity and its coordination with frontal systems were

particularly prominent, while peri-target beta differences suggested an additional contribution from earlier processing states. These findings provide temporal and network correlates of temporal-order accuracy, highlighting later right posterior activity and frontal–occipital coordination.

The ERP findings did not support the specific neural predictions derived from prior-entry and temporal integration accounts in the present task. Prior-entry accounts attribute reversals to the time course of attentional enhancement: the boost triggered by T1 develops with a delay and may reach its peak during T2 processing, allowing T2 to enter working memory first (e.g., refs. [6,7]). Relevant bilateral RSVP studies found that successive targets at the same location could elicit a single N2pc at onset separations of 120–150 ms, whereas a second N2pc re-emerged when the separation increased to 300 or 600 ms [37,38]. These findings are consistent with successive targets sharing spatial attentional engagement. Although behavioral effects of target cueing support the contribution of attentional dynamics to report order (e.g., refs. [6,8,39]), CO and OR trials did not reliably differ in N2pc onset latency or mean amplitude, and single-trial N2pc amplitude was not reliably associated with reversal probability. Temporal integration accounts propose that adjacent targets are jointly encoded within a common attentional episode, preserving their identities while weakening their temporal distinction (e.g., refs. [4,11,12]). Composite-percept reports and more frequent reversals for targets from the same category suggest that relationships between target representations

influence integration [13,14]. Our finding of more frequent reversals for numerically proximal targets is compatible with this view. Explicit integration has also been associated with smaller P3b responses, interpreted as reflecting reduced consolidation demands [15]. However, P3b amplitude neither differed reliably between CO and OR trials nor showed a reliable single-trial association with reversal probability; its interaction with numerical distance was also nonsignificant. The behavioral distance effect may therefore involve processes not captured by P3b amplitude. Overall, the ERP measures examined here provided no corresponding neural support for the predictions derived from these accounts.

The phase analyses also failed to support the predictions drawn from related areas of perception and sequence memory. Previous studies have linked prestimulus phase to visual detection, temporal integration, and tactile-order judgments (e.g., refs. [22–24,40]), while theta–gamma coupling strength has been associated with ordering demands and performance in working memory (e.g., refs. [27,28]). Here, the POS analyses identified no reliable pretarget phase difference, and neither theta- nor delta-based erPAC reliably distinguished CO from OR trials. These results provided no evidence that the measured pretarget phase or coupling-strength differences explained order reversals in this task. One possible reason is that the earlier findings reflect processes with different task demands: phase effects in visual detection may reflect fluctuations in stimulus detectability (e.g., refs. [22,23]); crossed-hand tactile

judgments involve remapping between anatomical and external spatial coordinates; and coupling during working-memory tasks may support the sustained maintenance and updating of ordered information (e.g., refs. [27,28]). Such findings may therefore not transfer directly to temporal-order processing during rapid visual presentation.

The ON400 findings identified a late posterior ERP component associated with temporal-order accuracy, with source estimates implicating right posterior cortex. CO trials elicited a more negative ON400 approximately 392–476 ms after T1 onset, and its amplitude was associated with report outcome at the single-trial level. Control comparisons suggested that this pattern was not readily explained solely by target load or identity-report success; a corresponding difference between order-preserving and reversed target–distractor reports further linked the response to the temporal relation between successfully reported items. The estimated sources spanned right posterior visual and association cortices, including occipital, inferior parietal, temporoparieto-occipital, and lateral temporal regions. This distribution is broadly compatible with lesion and TMS evidence implicating right posterior cortex in visual temporal-order judgments [16–18]. Complementary fMRI evidence identified bilateral posterior involvement, including the right temporoparietal junction and posterior inferior temporal cortex [41]. The present findings add an electrophysiological time course to this anatomical evidence and connect posterior activity to whether event order remains accurately

reportable despite successful identity report. The ON400 thus provides a candidate neural correlate of temporal organization at a later stage of visual processing.

Accurate order reports were associated with higher right posterior power both around target presentation and at later intervals, suggesting contributions from peri-target processing and later retention. The peri-target 11–20-Hz difference extended over right posterior parietal and frontocentral electrodes. Its posterior distribution and direction are broadly consistent with higher parieto-occipital alpha/low-beta power accompanying accurate visual temporal-order judgments [42]. Together with evidence that beta-frequency influences convey task context to visual cortex [43], this pattern suggests that a favorable attentional state around target presentation may help differentiate rapidly successive inputs. Later beta differences, approximately 650–800 ms after T1 onset, were most pronounced over right lateral occipitotemporal electrodes. Previous working-memory studies found greater posterior beta power when participants maintained the order of objects than when they maintained their spatial locations [44,45]. This comparison suggests that the present late beta activity may help keep temporal relations available after the targets have disappeared, supporting the subsequent order report. The later theta–alpha difference, approximately 800–960 ms, extended across right occipital, parietal, and temporal electrodes. Evidence linking theta activity to temporal-information maintenance and posterior alpha to the protection of

retained information [45,46] suggests that this activity may help maintain the target sequence in the presence of distractor-related interference. Numerical distance further moderated the early beta and late theta–alpha associations: higher power was more strongly associated with lower reversal probability for numerically distant pairs. One possibility is that more distinguishable numerical representations allow favorable early processing states and later maintenance to benefit order reporting more consistently, whereas competition between numerically proximal targets limits these benefits. Target relationships may therefore shape the contribution of oscillatory activity both around presentation and during later retention.

Accurate order reports were also accompanied by more consistent post-target low-frequency responses and stronger coordination between frontal and right occipital electrodes. The phase-consistency difference was most pronounced at 1–4 Hz approximately 150–850 ms after T1 onset and involved frontal, bilateral occipital, and right temporoparietal electrodes. At a later interval, approximately 530–860 ms, CO trials showed stronger 2–3-Hz synchronization between frontal and right occipital electrode groups. At these frequencies, right-occipital activity showed a phase lead relative to frontal activity in both conditions. Previous work has associated low-frequency phase alignment with improved visual processing under temporal regularities [47,48], and temporal-order judgments have also been linked to frontal–posterior coordination in audiovisual and tactile paradigms [49,50]. These findings suggest

that accurate temporal judgments can involve coordinated activity across distributed systems. In the present rapid sequence, more consistent event-locked responses may provide a stable temporal context for organizing successive targets, while later frontal–right-occipital synchronization may help maintain and use the resulting temporal relations for report. The right-occipital phase lead is also compatible with posterior representations providing a temporal reference for frontal processes involved in the later use of event relations. The regional phase-consistency and connectivity findings thus connect the reliability of post-target processing with the coordination of posterior representations and frontal systems.

These findings add temporal and network evidence to the visual “when” framework. Earlier work emphasized the contribution of right posterior systems to representing visual event timing [1,51]. The present study links this anatomical framework to the neural dynamics associated with preserving the order of identified events. The ON400, late right posterior power, and frontal–right-occipital synchronization together suggest that accurate sequence report may involve continued processing of temporal relations after the events themselves have disappeared. A favorable state around presentation may help differentiate successive inputs, while later posterior activity may support the preservation of their temporal relations and frontal–posterior coordination may support their subsequent use. This interpretation places later right posterior processing and its coordination with frontal systems at the center of

598 a working account of temporal-order accuracy. The present findings therefore
599 connect visual “when” processing with the maintenance and later use of event
600 sequences, providing candidate neural processes for why knowing event
601 identities does not guarantee an accurate account of their order.

602 Several questions remain. First, the role of spatial location is unresolved.
603 The lower reversal probability in the right visual field was directionally
604 consistent with right-field advantages in basic visual temporal discrimination [52],
605 but differed from left-field advantages in simultaneity and temporal-order
606 precision [31] and in T2 identification during dual-stream RSVP [53]. These tasks
607 differ in stimulus arrangement, judgment demands, and behavioral measures;
608 the present neural analyses did not explain the mechanism underlying our
609 visual-field asymmetry. Second, the present analyses primarily characterized
610 responses to the target pair and could not resolve the finer processing of T1
611 and T2 or their interaction. Third, template-based source reconstruction has
612 limited anatomical precision, leaving the specific cortical origins of the right
613 posterior effects to be established with more precise measurements. The lack
614 of support for several predictions from related paradigms suggests that those
615 neural signatures may not transfer directly to rapid visual sequences. Equally,
616 whether the right posterior and frontal–occipital features identified here
617 generalize to other temporal intervals, spatial arrangements, and sensory
618 modalities remains to be tested. Future work combining target-specific neural
619 measurements, systematic comparisons across tasks and visual fields, and

controlled perturbation of posterior regions could clarify how individual events acquire and retain their temporal positions. Successful identification does not guarantee accurate order report; the present findings link this distinction to later right posterior processing and its coordination with frontal systems.

Methods

Participants

A total of 31 right-handed individuals with normal or corrected-to-normal vision and no self-reported history of psychiatric, neurological, or other major medical conditions were recruited from the university campus and surrounding community using convenience sampling. The target sample size of 30 was determined before data collection based on sample sizes used in closely related studies (15–19 participants per experiment in Zhou et al.[14]; 32 participants in Akyürek et al.[15]). No formal a priori power analysis was conducted. Four participants were excluded because of excessive EEG artifacts according to the predefined exclusion criteria described below. The final sample comprised 27 participants (16 female and 11 male), aged 19–24 years (M = 20.36, SD = 1.45), all of whom were included in the behavioral and EEG analyses. Sex and handedness were self-reported. All participants provided written informed consent before participation and received monetary compensation at a rate of CNY 60 per hour. The study was conducted in

accordance with the Declaration of Helsinki and was approved by the Ethics Committee of the Faculty of Psychology at Southwest University (approval no. H22049).

Experimental design

Participants were tested individually in a sound-attenuated room. Stimuli were presented on a black background on an LED monitor (1024 × 768 pixels, 60 Hz refresh rate) at a viewing distance of approximately 60 cm. Stimulus presentation and response collection were controlled using E-Prime 2.0 (RRID:SCR_009567; Psychology Software Tools, Pittsburgh, PA).

As shown in **Fig. 1a**, each trial began with a central fixation cross (gray, 0.75° × 0.75°) presented for 800 ms. Two lateral RSVP streams were then presented while the fixation cross remained visible throughout the sequence. Each stream consisted of 10–13 frames, with each frame containing one alphanumeric character in each visual field. Characters subtended approximately 1° in height, and the two streams were separated by 3.5° center to center. Each frame was displayed for 100 ms with no interstimulus interval.

Within each trial, digits were selected without replacement from the eight possible values ranging from 2 to 9. Across the two streams, letter distractors were randomly selected without replacement from 22 uppercase English letters, excluding B, I, O, and Z to minimize visual ambiguity between letters

and digits. If more than 22 letter distractors were required within a trial, the letter pool was replenished after all 22 letters had been used, and sampling continued without replacement. Distractors were displayed in gray, whereas target digits were presented in one of three colors randomly selected on each trial: blue (RGB: 81, 174, 226), green (RGB: 46, 175, 68), or orange (RGB: 234, 105, 30).

T1 appeared with equal probability in the left or right RSVP stream and could occur in the fifth, sixth, seventh, or eighth frame of the sequence. The contents of the immediately following frame determined the experimental condition. The experiment comprised three conditions: T, TD, and TT. In the T condition, the item following T1 at the target location was a gray letter distractor, as was the simultaneously presented item in the contralateral stream. In the TD condition, a gray digit distractor appeared at Lag 1 in the same stream as T1, while a gray letter appeared in the contralateral stream. In the TT condition, T2 appeared at Lag 1 in the same stream and in the same color as T1, while the contralateral stream again contained a gray letter.

Participants were informed before the experiment that whenever two colored targets were presented, T1 and T2 would always appear at the same spatial location, would always be presented in the same color, and would always be different digits. The three conditions were presented in a 1:4:5 ratio (T:TD:TT), such that trials containing one colored target and those containing two colored targets occurred with equal overall probability; participants were

also informed of this distribution. Four additional distractor frames followed the frame immediately after T1. Trials were pseudorandomized separately for each participant in sets of 10, with each set comprising one T trial, four TD trials, and five TT trials. Trial order within each set was randomized. Target visual field and T1 serial position were balanced within each condition across the experimental session, whereas target color was distributed as evenly as possible. Digit identities were randomly selected subject to the no-replacement constraint described above.

After the RSVP sequence, the fixation cross remained on the screen for 500 ms. Two separate response screens were then presented sequentially. The first screen prompted participants to report T1 by pressing one of the number keys from 2 to 9 on a standard computer keyboard. The second screen prompted them to report T2 by pressing a number key from 2 to 9 or, when no second colored target had been presented, the space bar. Responses were self-paced, with no response deadline, but participants were required to respond on both screens before the trial could proceed. Each trial ended with an 800-ms blank screen.

Participants completed 20 practice trials before the formal experiment. The experimental session comprised 1,000 trials divided into 10 blocks of 100 trials each, with self-paced breaks between blocks. The session therefore included 100 T trials, 400 TD trials, and 500 TT trials.

EEG recording and preprocessing

The EEG data were recorded using a standard 64-channel Ag/AgCl electrode cap (Neuroscan Quik-Cap) arranged according to the extended international 10–20 system. Vertical and horizontal electrooculographic signals were recorded simultaneously with electrodes placed below the left eye and at the outer canthus of the right eye, respectively. During acquisition, all channels were referenced to an electrode located near the vertex. EEG signals were continuously sampled at 1000 Hz and online band-pass filtered between 0.1 and 100 Hz. Electrode impedances were maintained below 10 kΩ throughout the recording.

EEG preprocessing was performed in MATLAB R2023b (RRID:SCR_001622; The MathWorks Inc., 2023) using the EEGLAB toolbox (RRID:SCR_007292) [54]. First, line noise was attenuated using Zapline-plus [55,56] (https://github.com/MariusKlug/zapline-plus) and CleanLine (RRID:SCR_002233) [57]. The continuous data were then high-pass filtered at 0.25 Hz and low-pass filtered at 70 Hz using zero-phase finite-impulse-response (FIR) filters. Bad channels were identified using the clean_rawdata plugin [58] (https://github.com/sccn/clean_rawdata) and temporarily removed based on flatline periods longer than 5 s, line-noise contamination exceeding 4 *SD*, or a channel-correlation criterion of 0.80. The data were subsequently downsampled to 250 Hz.

ICA was performed on a copy of the continuous data high-pass filtered at 1 Hz, and the resulting decomposition was applied to the corresponding data

high-pass filtered at 0.25 Hz. Components classified by ICLabel [59] (https://github.com/sccn/ICLabel) as eye, muscle, or channel-noise components with a probability greater than 0.90 were removed.

For ERP analyses, the data were additionally low-pass filtered at 40 Hz before being segmented into epochs extending from −200 to 800 ms relative to T1 onset. For time–frequency analyses, the 70-Hz low-pass-filtered data were segmented into extended epochs from −2000 to 3000 ms relative to T1 onset to minimize edge artifacts during spectral decomposition. Time-domain baseline correction was performed by subtracting the mean voltage during the −200 to 0 ms interval from each epoch. Artifact rejection was conducted within the −200 to 800 ms interval relative to T1 onset; epochs were rejected if the voltage exceeded ±75 μV within this interval. Bad channels were reconstructed using spherical spline interpolation, and the data were re-referenced to the average of all EEG channels.

Four participants were excluded from further analyses because more than 40% of trials in the conditions included in the primary analyses were rejected due to artifacts. Among the remaining 27 participants, an average of 3.61% (*SD* = 4.82%) of trials were rejected because of artifacts, and an average of 2.59 (*SD* = 1.58) channels per participant were identified as bad.

ERP analysis

ERPs were averaged separately for each participant and condition and

749 analyzed using ERPLAB (RRID:SCR_009574) [60]. The N2pc was measured
750 from contralateral-minus-ipsilateral difference waveforms at PO7/PO8 relative
751 to target location, whereas P3b amplitude was measured by averaging activity
752 across Pz, P1, and P2. Mean amplitudes were calculated within 200–260 ms
753 for the N2pc and 300–450 ms for the P3b after T1 onset. These electrode
754 sites and time windows were selected based on previous literature (e.g.,
755 ref. [61]) and the condition-collapsed grand-average waveforms.

756 The ON400 was identified as an exploratory, data-driven effect using a
757 cluster-based permutation analysis comparing posterior ERP activity between
758 CO and OR trials. For descriptive quantification, mean ON400 amplitude was
759 extracted from Oz, O1, and O2 within the cluster-defined interval (392–476
760 ms after T1 onset). Control comparisons contrasted DI_TD with DI_DT trials
761 within the TD condition, correct T trials with CO trials, and CO trials with TT
762 trials in which only one target identity was correctly reported. The same
763 electrode set and time window, defined exclusively by the original CO–OR
764 comparison, were applied to all control comparisons without further selection.
765 For each comparison, participants were required to contribute at least 15
766 artifact-free trials to each of the two compared conditions. Participant eligibility
767 was determined separately for each comparison.

768 N2pc onset latency was operationalized using the 25% fractional-area
769 latency method. To improve the signal-to-noise ratio, the N2pc difference
770 waveforms were low-pass filtered at 10 Hz specifically for latency estimation.

Latencies were calculated using a jackknife procedure [62], in which leave-one-participant-out grand-average waveforms were generated iteratively for each condition. The 25% fractional-area latency was defined as the time point at which the cumulative N2pc area reached 25% of the total area within the 175–300-ms interval after T1 onset. Condition differences were evaluated using a paired-samples *t* test on the jackknife estimates. The resulting *t* statistic was divided by $N - 1$ and evaluated with $N - 1$ degrees of freedom, where N denotes the number of participants [62].

Source localization analysis

To estimate the cortical sources associated with the sensor-level ON400 effect, cortical source reconstruction was performed separately for each participant and condition using MNE software (RRID:SCR_005972) [63]. Source models were constructed using the FreeSurfer fsaverage template anatomy (RRID:SCR_001847) [64]. The cortical source space was defined using the precomputed ico-5 cortical surface source space, and the forward solution was constructed using a three-layer boundary-element model comprising the brain, skull, and scalp. Source locations within 5 mm of the inner-skull surface were excluded from the forward solution. The noise covariance matrix was estimated from the −200 to 0 ms interval relative to T1 onset. Cortical activity was then reconstructed using sLORETA with a loose orientation constraint of 0.2, depth weighting of 0.8, and a regularization parameter corresponding to an assumed signal-to-noise ratio of 3 [65].

For each participant and condition, source estimates were averaged over the ON400 interval of 392–476 ms after T1 onset, and the CO–OR difference was calculated at each source location. Condition differences across participants were assessed using a nonparametric spatial cluster-based permutation test based on cortical-surface adjacency, thereby controlling for multiple comparisons across source locations. The sensor-defined time window was held fixed for all source-space comparisons. Significant clusters were anatomically characterized using the Destrieux cortical parcellation (aparc.a2009s) [66].

Time-frequency analysis

EEG epochs were decomposed into time–frequency representations spanning 1–70 Hz in nominal 1-Hz steps using adaptive additive superlets [67]. Superlet order increased linearly with frequency from 1 at 1 Hz to 10 at 70 Hz, with a 3-cycle base Morlet wavelet. Power was calculated as the squared magnitude of the complex time–frequency coefficients. Time–frequency decomposition was implemented using FieldTrip (RRID:SCR_004849) [68]. Power analyses focused on the 1–40 Hz range. For condition-level analyses, power was first averaged across trials within each condition for each participant and then baseline-normalized and expressed in decibels. For single-trial analyses, power was baseline-normalized and expressed in decibels separately for each trial, electrode, and frequency, using that trial's mean baseline power. Both analyses used the −500 to −200 ms interval relative to T1 onset as the

baseline.

Condition-level power was analyzed across 10 predefined ROIs, comprising seven regional ROIs and three lateralized contralateral-minus-ipsilateral ROIs (**Supplementary Fig. 4**). The regional ROIs covered the frontal pole, left and right fronto-central regions, the fronto-central and centro-parietal midlines, and left and right posterior regions. Lateralized power was calculated as contralateral minus ipsilateral power for homologous electrode groups spanning anterior, central, and posterior regions, with laterality defined relative to the target visual field. Particular attention was given to the right posterior ROI (CP4, CP6, TP8, P4, P6, P8, PO4, PO6, PO8, and O2), motivated by previous lesion and TMS evidence implicating right posterior cortex in visual temporal-order judgments (e.g., refs. [16–18]) and by the source estimates of the ON400 effect. For each ROI, power was averaged across its constituent electrodes before statistical analysis. CO–OR differences were assessed using cluster-based permutation tests, with multiple comparisons across time–frequency samples controlled separately within each ROI. For descriptive follow-up analyses, mean power was extracted from time–frequency intervals encompassing the significant effects and from electrode clusters identified in subsequent spatial analyses.

For the single-trial GLMMs, mean baseline-normalized power was extracted for each trial from the corresponding spatial electrode clusters within three time–frequency windows: 10–20 Hz from −130 to 150 ms, 12–20 Hz

from 680 to 790 ms, and 4–12 Hz from 800 to 930 ms relative to T1 onset. These values were retained at the trial level for subsequent modeling.

Inter-trial phase coherence analysis

Single-trial phase information was extracted from the complex-valued output of the superlet time–frequency analysis described above. For each participant and condition, ITPC was computed at each electrode, time point, and frequency to quantify phase consistency across trials. Specifically, at each time point t and frequency f, ITPC was calculated as the magnitude of the circular mean of phase vectors across N trials for each condition:

$$ITPC(t,f) = \left| \frac{1}{N} \sum_{k=1}^{N} e^{i\theta_{k(t,f)}} \right|,$$

where $\theta_k(t, f)$ denotes the phase angle of trial k, and N is the number of trials included in the estimate. ITPC values range from 0 to 1, with higher values indicating stronger phase consistency across trials and lower values reflecting greater phase variability.

Because ITPC estimates are sensitive to trial count, with fewer trials tending to produce inflated estimates, trial numbers were matched between CO and OR conditions using random subsampling before ITPC estimation. For each participant, ITPC was calculated using all available artifact-free trials in the condition with fewer observations. Trials from the other condition were randomly sampled without replacement to match this trial count. ITPC was calculated for each of 1,000 subsamples, and these estimates were averaged

858 to obtain the trial-count-matched estimate for that condition. Finally, the CO–
859 OR ITPC difference was calculated for each participant and submitted to
860 subsequent statistical analyses.

861 As a complementary measure of inter-trial phase consistency, we also
862 computed PPC [69], which provides an estimate without finite-sample bias
863 related to trial number. PPC was calculated using all available artifact-free
864 trials in each condition, without trial-count matching. Unlike ITPC, which is
865 based on the resultant vector across all trials, PPC is calculated from the
866 average pairwise similarity between phase angles across trials. Specifically,
867 for a set of phase angles $\{\theta_1, \theta_2, \ldots, \theta_N\}$, the sample estimate of PPC is
868 defined as:

869 $$\mathrm{PPC} = \frac{2}{N(N-1)} \sum_{j=1}^{N-1} \sum_{k=j+1}^{N} \cos(\theta_j - \theta_k),$$

870 where $\cos(\theta_j - \theta_k)$ represents the cosine of the phase difference between
871 trials j and k. Because PPC is not systematically inflated by smaller trial
872 counts, it was used to assess the robustness of the CO–OR comparison to
873 the choice of phase-consistency estimator.

874 For the primary time–frequency comparisons, ITPC and PPC were
875 calculated separately at each electrode and then averaged across all scalp
876 electrodes. CO–OR differences were assessed over 1–40 Hz and −500 to
877 1000 ms relative to T1 onset using cluster-based permutation tests.

Phase-opposition sum analysis

To examine whether CO and OR trials were associated with distinct prestimulus oscillatory phases, POS [70] was computed from single-trial phase estimates. For this analysis, the EEG data were separately decomposed using 3-cycle Morlet wavelets from 2 to 40 Hz in nominal 1-Hz steps. Single-trial phase angles extracted from the complex-valued time–frequency coefficients were used for subsequent analyses.

For each participant, electrode, time point, and frequency, POS was computed as:

$$\mathrm{POS} = \mathrm{ITPC}_{\mathrm{CO}} + \mathrm{ITPC}_{\mathrm{OR}} - 2\mathrm{ITPC}_{\mathrm{all}},$$

where $\mathrm{ITPC}_{\mathrm{CO}}$ and $\mathrm{ITPC}_{\mathrm{OR}}$ denote the inter-trial phase coherence computed separately for CO and OR trials, respectively, and $\mathrm{ITPC}_{\mathrm{all}}$ denotes the ITPC computed after pooling trials across both conditions. Higher POS values reflect greater average phase concentration within conditions relative to the pooled trials. Evidence for outcome-related phase separation was assessed against a label-shuffled null distribution.

Because POS can be affected by unequal trial numbers, CO and OR trial counts were matched using random subsampling. For each participant, 3,000 trial-matching iterations were performed. In each iteration, all trials from the condition with fewer observations were retained, and trials from the larger condition were randomly sampled without replacement to match this trial

count. POS was calculated from the matched trials. The condition labels of the same matched trials were then shuffled once, preserving equal trial counts, to generate a corresponding null POS value. The observed POS was defined as the mean across the 3,000 trial-matching iterations, and the 3,000 shuffled POS values formed the null distribution. The observed POS was then standardized relative to this distribution:

$$z\mathrm{POS} = \frac{M_{\mathrm{POS,obs}} - M_{\mathrm{POS,shuffle}}}{SD_{\mathrm{POS,shuffle}}},$$

where $M_{\mathrm{POS,obs}}$ denotes the mean observed POS across the 3,000 trial-matching iterations, and $M_{\mathrm{POS,shuffle}}$ and $SD_{\mathrm{POS,shuffle}}$ denote the mean and standard deviation of the 3,000 shuffled POS values, respectively. Positive zPOS values indicate that observed POS exceeded the mean of the shuffled distribution.

POS analyses were restricted to the prestimulus interval from −700 to 0 ms relative to T1 onset. To reduce contamination from post-target activity caused by wavelet temporal smearing, time–frequency points satisfying $t > -\frac{1.5}{f}$, where *t* is time in seconds relative to T1 onset and *f* is frequency in Hz, were excluded before statistical testing. This criterion excluded points within 1.5 cycles of T1 onset, corresponding to 500 ms at 3 Hz, 375 ms at 4 Hz, and 150 ms at 10 Hz. Only the remaining time–frequency samples were included in the group analyses.

The primary analysis focused on the parieto-occipital ROI comprising P1,

Pz, P2, PO3, POz, PO4, PO5, PO6, PO7, PO8, O1, Oz, and O2. zPOS was computed separately at each electrode and then averaged within this ROI for each participant. A supplementary analysis averaged electrode-level zPOS across all scalp electrodes. In both analyses, the time–frequency samples remaining after applying the temporal-smearing exclusion criterion were compared against zero using two-sided cluster-based permutation tests.

Event-related phase–amplitude coupling analysis

erPAC was computed to quantify the across-trial association between low-frequency phase and higher-frequency amplitude at each time point [71]. Low-frequency phase was extracted separately from the delta (1–4 Hz) and theta (4–7 Hz) bands. The EEG signal was band-pass filtered within each phase-frequency band using a bidirectional zero-phase FIR filter. The analytic signal was obtained using the Hilbert transform, and instantaneous phase was extracted as the phase angle of the resulting complex signal. Higher-frequency amplitude was obtained as the magnitude of the complex superlet coefficients described above. Amplitude frequencies ranged from 5 to 70 Hz for the delta-phase analysis and from 8 to 70 Hz for the theta-phase analysis, both in nominal 1-Hz steps.

For each participant, condition, electrode, time point, phase band, and amplitude frequency, erPAC was calculated as the circular–linear correlation between single-trial low-frequency phase and higher-frequency amplitude

across trials:

$$\mathrm{erPAC}(t, B_\phi, f_a) = \rho_{\mathrm{cl}}\left[\phi(t, B_\phi), A(t, f_a)\right],$$

where B_ϕ denotes the phase band, f_a denotes the amplitude frequency, $\phi(t, B_\phi)$ denotes the single-trial phase angle, $A(t, f_a)$ denotes the corresponding single-trial amplitude envelope, and ρ_{cl} denotes the circular–linear correlation coefficient:

$$\rho_{\mathrm{cl}} = \sqrt{\frac{r_{Ac}^2 + r_{As}^2 - 2r_{Ac}r_{As}r_{cs}}{1 - r_{cs}^2}},$$

where r_{Ac} and r_{As} are the Pearson correlation coefficients between amplitude and $\cos\phi$ and between amplitude and $\sin\phi$, respectively, and r_{cs} is the Pearson correlation coefficient between $\cos\phi$ and $\sin\phi$.

Because erPAC estimates may be sensitive to unequal trial numbers, CO and OR trial counts were matched by random subsampling before erPAC estimation. For each participant, 1000 trial-matching iterations were performed. In each iteration, all trials from the condition with fewer observations were retained, and trials from the larger condition were randomly sampled without replacement to match this trial count. Phase and amplitude estimates from corresponding trials were selected together, and erPAC was calculated separately for CO and OR trials. The resulting estimates were then averaged across iterations for each condition. Electrode-level CO–OR differences were averaged across all scalp electrodes and evaluated over

−500 to 1000 ms relative to T1 onset using separate cluster-based permutation tests for the delta- and theta-phase analyses.

Functional connectivity analysis

Phase information for the FC analyses was obtained from the complex-valued coefficients generated by the superlet time–frequency decomposition described above. The dwPLI and dPLI were calculated to characterize non-zero-lag phase synchronization and phase-leading asymmetry, respectively [35,36]. dwPLI quantifies the consistency of non-zero-lag phase relationships while weighting observations by the magnitude of the imaginary component of the cross-spectrum and reducing finite-sample bias. dPLI retains information about the sign of the phase lag, thereby indicating which **electrode** group preferentially phase leads the other, without implying causal or directed information flow.

FC was calculated between a frontal ROI comprising F1, F2, Fz, FC1, FC2, and FCz and two lateral occipital ROIs. The left occipital ROI comprised PO7, PO5, PO3, and O1, whereas the right occipital ROI comprised PO8, PO6, PO4, and O2. For each hemisphere, all 24 possible frontal–occipital electrode pairs were included. Connectivity measures were first calculated separately for each electrode pair and then averaged across the 24 pairs to obtain frontal–left-occipital and frontal–right-occipital estimates for each participant and condition. The dwPLI analysis covered 1–40 Hz and −500 to

1000 ms relative to T1 onset, with the two networks tested separately. CO–OR differences were assessed using cluster-based permutation testing.

For the dwPLI analysis, the complex cross-spectrum was first calculated for each trial n, frequency f, time point t, and frontal–occipital electrode pair (i, j):

$$S_{ij,n}(f,t) = Z_{i,n}(f,t)Z^{*}_{j,n}(f,t),$$

where $Z_{i,n}(f,t)$ and $Z_{j,n}(f,t)$ denote the complex superlet coefficients at the frontal and occipital electrodes, respectively, and the asterisk denotes complex conjugation. The imaginary component of the cross-spectrum was defined as

$$I_{ij,n}(f,t) = \mathrm{Im}\left[S_{ij,n}(f,t)\right].$$

dwPLI was then calculated across trials using the debiased weighted estimator:

$$\mathrm{dwPLI}_{ij}(f,t) = \frac{\left[\sum_{n=1}^{N} I_{ij,n}(f,t)\right]^2 - \sum_{n=1}^{N} I_{ij,n}^2(f,t)}{\left[\sum_{n=1}^{N} \left| I_{ij,n}(f,t) \right|\right]^2 - \sum_{n=1}^{N} I_{ij,n}^2(f,t)},$$

where N denotes the number of trials. This formulation reduces the positive bias in squared weighted phase-lag estimates arising from a finite number of observations. dwPLI was calculated using all available artifact-free trials in each condition, without trial-count matching.

As an exploratory follow-up to the dwPLI results, dPLI was examined at

the nominal 2- and 3-Hz frequency bins. Phase-leading asymmetry was calculated from the sign of the imaginary component of the same trial-wise cross-spectrum:

$$\mathrm{dPLI}_{ij}(f,t) = \frac{1}{N}\sum_{n=1}^{N} H\left[I_{ij,n}(f,t)\right],$$

where

$$H(x) = \begin{cases} 1, & x > 0, \\ 0.5, & x = 0, \\ 0, & x < 0. \end{cases}$$

With the frontal electrode defined as i and the occipital electrode as j, dPLI values greater than 0.5 indicate preferential frontal phase leading, values below 0.5 indicate preferential occipital phase leading, and a value of 0.5 indicates no consistent phase-leading asymmetry. To control for unequal trial numbers, CO and OR trials were matched using random subsampling. For each participant, 1,000 trial-matching iterations were performed. In each iteration, all trials from the condition with fewer observations were retained, and trials from the larger condition were randomly sampled without replacement to match this trial count. dPLI was calculated separately for CO and OR trials. The resulting estimates were averaged across iterations and across these two frequency bins and 24 electrode pairs to obtain a time course for each network. Cluster-based permutation tests compared CO with OR and each condition with the reference value of 0.5.

Single-trial analysis

To characterize trial-level associations between behavioral and neural measures and temporal-order outcome, we fitted a series of GLMMs. Only CO and OR trials were included. The binary dependent variable was coded as 1 for OR trials and 0 for CO trials. Target visual field (left vs. right) was coded using sum-to-zero contrasts (left = −0.5; right = +0.5), whereas all continuous predictors—including absolute numerical distance, single-trial ERP amplitudes, and single-trial time–frequency power—were z-standardized across trials and participants within each analysis dataset before model fitting. All models assumed a binomial error distribution with a logit link and included a participant-specific random intercept to account for repeated observations and inter-individual variability. GLMMs were estimated by maximum likelihood using the default Laplace approximation implemented in the *glmer* function of the lme4 package (RRID:SCR_015654), and fixed effects were evaluated using two-sided Wald *z* tests [72].

Separate models were first fitted for each behavioral or neural predictor. The behavioral models included either target visual field or the absolute numerical distance between T1 and T2 as the predictor. Single-trial ERP amplitudes were extracted from the electrode sets described above within 200–260 ms for the N2pc, 300–450 ms for the P3b, and 392–476 ms for the ON400. Single-trial power was baseline-normalized before averaging within the electrode sets and time–frequency windows used to characterize the corresponding effects: 10–20 Hz at −130 to 150 ms for early beta, 12–20 Hz

at 680–790 ms for late beta, and 4–12 Hz at 800–930 ms for late theta–alpha. All time intervals were relative to T1 onset. Each model was specified as

$$\text{logit}\left[P\left(Y_{kp}=1\right)\right]=\beta_0+\beta_1X_{kp}+u_{0p},$$

where Y_{kp} denotes the response outcome on trial k for participant p, X_{kp} denotes the predictor of interest, β_0 and β_1 denote the fixed intercept and slope, respectively, and u_{0p} denotes the participant-specific random intercept, with $u_{0p}\sim N(0,\sigma_u^2)$. For continuous predictors, β_1 represents the change in the log odds of an OR response associated with a 1-*SD* increase in the predictor, and $\exp(\beta_1)$ gives the corresponding odds ratio.

To determine whether the associations between neural activity and order reversal varied as a function of target visual field or numerical distance, additional GLMMs were fitted for each ERP and time–frequency measure. Each ERP and time–frequency measure was entered into two separate interaction models: one containing its interaction with target visual field and the other containing its interaction with standardized absolute numerical distance. Both main effects were included in each model:

$$\text{logit}\left[P\left(Y_{kp}=1\right)\right]=\beta_0+\beta_1X_{kp}+\beta_2M_{kp}+\beta_3X_{kp}M_{kp}+u_{0p},$$

where X_{kp} denotes the neural predictor, M_{kp} denotes either target visual field or numerical distance, and β_3 represents the interaction effect. For each model, the interaction coefficient, SE, Wald z statistic, p value, and odds ratio $\exp(\beta_3)$ were extracted. Significant interactions were followed by simple-slope

analyses. For significant interactions with numerical distance, neural slopes were evaluated at standardized numerical distances of −1, 0, and +1, corresponding to one *SD* below the mean, the mean, and one *SD* above the mean, respectively; these values were evaluation points on a continuous moderator rather than separate trial groups. Follow-up *p* values were adjusted using the Holm procedure within each set of three slopes. Because the ON400 and oscillatory features were selected using the same CO–OR dataset, their single-trial associations were treated as exploratory rather than independent validation of these effects.

Statistics and Reproducibility

Conventional frequentist and Bayesian statistical analyses were conducted in JASP (RRID:SCR_015823) [73]. When the assumption of sphericity was violated, Greenhouse–Geisser-corrected degrees of freedom and *p* values were reported. Pairwise post hoc comparisons following significant ANOVA effects were adjusted using the Holm procedure. Effect sizes were quantified using ω^2 for repeated-measures ANOVAs and Cohen's *d* for *t* tests. For Bayesian analyses, the strength of evidence was summarized using Bayes factors (BF_{01} or BF_{10}, as appropriate).

To quantify the behavioral trend across numerical distances, an ordinary least-squares regression was fitted separately for each participant to the seven distance-specific order-reversal percentages as a function of absolute

numerical distance (1–7). Each percentage used all TT trials at that distance as its denominator. The resulting participant-level slopes were compared against zero using a two-sided one-sample *t* test. The reported coefficient *b* is the mean slope, expressed in percentage points per unit of numerical distance, and its *SE* was calculated across participants.

Cluster-based nonparametric permutation tests were implemented in FieldTrip to evaluate condition differences in ERP amplitudes, time–frequency power, ITPC, PPC, POS, erPAC, dwPLI, and dPLI, as well as their corresponding scalp topographies [68,74]. At each electrode, time point, or time–frequency sample, paired-samples *t* tests were used for comparisons between CO and OR, whereas one-sample *t* tests were used when participant-level values were compared against a reference value, such as zero. Samples exceeding a two-sided cluster-forming threshold of $p < 0.05$ were grouped according to their temporal, spectral, or spatial adjacency, and the sum of the *t* statistics within each cluster was used as the cluster-level statistic. For scalp analyses, spatial adjacency was defined using a triangulation-based neighborhood structure, in which electrodes were connected according to their relative positions in the sensor layout, and channels sharing an edge in the resulting triangulation were treated as spatial neighbors. Statistical significance was assessed against a Monte Carlo null distribution generated from 20,000 within-participant permutations, using condition-label exchanges or sign reversals of participant-level contrasts as appropriate. For each

permutation, the maximum absolute cluster statistic was retained to control the familywise error rate. Cluster-level *p* values were calculated as the proportion of permutation-derived maximum cluster statistics that were at least as extreme as the observed cluster statistic.

Data availability

The data supporting the findings of this study are publicly available on the Open Science Framework at https://osf.io/gb4uz.

Code availability

The analysis code supporting the findings of this study is publicly available on the Open Science Framework at https://osf.io/gb4uz.

Funding

This work was supported by grants from the National Natural Science Foundation of China to Antao Chen (grant numbers: 32171040 and 32371105).

Competing interests

The authors declare no competing interests.

Author contributions

Zong Meng: Conceptualization, Methodology, Investigation, Formal analysis,

Writing – original draft, Writing – review and editing. Qi Chen: Investigation, Formal analysis. Liqin Zhou: Writing – review and editing. Ke Zhou: Writing – review and editing. Antao Chen: Conceptualization, Methodology, Writing – review and editing.

References

1. Battelli, L., Pascual-Leone, A. & Cavanagh, P. The 'when' pathway of the right parietal lobe. *Trends Cogn. Sci.* **11**, 204–210 (2007).
2. Ding, N. Sequence chunking through neural encoding of ordinal positions. *Trends Cogn. Sci.* **29**, 641–654 (2025).
3. Chun, M. M. & Potter, M. C. A two-stage model for multiple target detection in rapid serial visual presentation. *J. Exp. Psychol. Hum. Percept. Perform.* **21**, 109–127 (1995).
4. Hommel, B. & Akyürek, E. G. Lag-1 sparing in the attentional blink: Benefits and costs of integrating two events into a single episode. *Q. J. Exp. Psychol. Sect. A* **58**, 1415–1433 (2005).
5. Visser, T. A. W., Bischof, W. F. & Di Lollo, V. Attentional switching in spatial and nonspatial domains: Evidence from the attentional blink. *Psychol. Bull.* **125**, 458–469 (1999).
6. Olivers, C. N. L., Hilkenmeier, F. & Scharlau, I. Prior entry explains order reversals in the attentional blink. *Atten. Percept. Psychophys.* **73**, 53–67 (2011).

7. Olivers, C. N. L. & Meeter, M. A boost and bounce theory of temporal attention. *Psychol. Rev.* **115**, 836–863 (2008).

8. Hilkenmeier, F., Olivers, C. N. L. & Scharlau, I. Prior entry and temporal attention: Cueing affects order errors in RSVP. *J. Exp. Psychol. Hum. Percept. Perform.* **38**, 180–190 (2012).

9. Zivony, A., Allon, A. S., Luria, R. & Lamy, D. Dissociating between the N2pc and attentional shifting: An attentional blink study. *Neuropsychologia* **121**, 153–163 (2018).

10. Zivony, A. & Eimer, M. Distractor intrusions are the result of delayed attentional engagement: A new temporal variability account of attentional selectivity in dynamic visual tasks. *J. Exp. Psychol. Gen.* **150**, 23–41 (2021).

11. Akyürek, E. G. Temporal integration as an adaptive process in visual perception, attention, and working memory. *Neurosci. Biobehav. Rev.* **170**, 106041 (2025).

12. Bowman, H. & Wyble, B. The simultaneous type, serial token model of temporal attention and working memory. *Psychol. Rev.* **114**, 38–70 (2007).

13. Akyürek, E. G. *et al.* Temporal target integration underlies performance at lag 1 in the attentional blink. *J. Exp. Psychol. Hum. Percept. Perform.* **38**, 1448–1464 (2012).

14. Zhou, L., Ding, J. & Zhou, K. Categorical similarity modulates temporal integration in the attentional blink. *J. Vis.* **20**, 9 (2020).

15. Akyürek, E. G., Kappelmann, N., Volkert, M. & Van Rijn, H. What You See Is What You Remember: Visual Chunking by Temporal Integration Enhances

Working Memory. *J. Cogn. Neurosci.* **29**, 2025–2036 (2017).

16. Rorden, C., Mattingley, J. B., Karnath, H.-O. & Driver, J. Visual extinction and prior entry: Impaired perception of temporal order with intact motion perception after unilateral parietal damage. *Neuropsychologia* **35**, 421–433 (1997).

17. Snyder, J. J. & Chatterjee, A. Spatial-temporal anisometries following right parietal damage. *Neuropsychologia* **42**, 1703–1708 (2004).

18. Woo, S.-H., Kim, K.-H. & Lee, K.-M. The role of the right posterior parietal cortex in temporal order judgment. *Brain Cogn.* **69**, 337–343 (2009).

19. Fiebelkorn, I. C. & Kastner, S. A Rhythmic Theory of Attention. *Trends Cogn. Sci.* **23**, 87–101 (2019).

20. Jensen, O. & Mazaheri, A. Shaping Functional Architecture by Oscillatory Alpha Activity: Gating by Inhibition. *Front. Hum. Neurosci.* **4**, (2010).

21. VanRullen, R. Perceptual Cycles. *Trends Cogn. Sci.* **20**, 723–735 (2016).

22. Busch, N. A., Dubois, J. & VanRullen, R. The Phase of Ongoing EEG Oscillations Predicts Visual Perception. *J. Neurosci.* **29**, 7869–7876 (2009).

23. Mathewson, K. E., Gratton, G., Fabiani, M., Beck, D. M. & Ro, T. To See or Not to See: Prestimulus α Phase Predicts Visual Awareness. *J. Neurosci.* **29**, 2725–2732 (2009).

24. Takahashi, T. & Kitazawa, S. Modulation of Illusory Reversal in Tactile Temporal Order by the Phase of Posterior α Rhythm. *J. Neurosci.* **37**, 5298–5308 (2017).

25. Lisman, J. E. & Idiart, M. A. Storage of 7 +/- 2 short-term memories in oscillatory subcycles. *Science* **267**, 1512–1515 (1995).

26. Lisman, J. E. & Jensen, O. The θ-γ neural code. *Neuron* **77**, 1002–1016 (2013).

27. Brooks, H. *et al.* Theta–gamma coupling and ordering information: a stable brain–behavior relationship across cognitive tasks and clinical conditions. *Neuropsychopharmacology* **45**, 2038–2047 (2020).

28. Rajji, T. K. *et al.* Ordering Information in Working Memory and Modulation of Gamma by Theta Oscillations in Humans. *Cereb. Cortex* bhv326 (2016) doi:10.1093/cercor/bhv326.

29. Luo, Y., He, Y. & Bao, Y. Perifoveal and peripheral attentional modulation on order perception. *PsyCh J.* **12**, 835–837 (2023).

30. Matthews, N., Welch, L., Festa, E. & Clement, A. Remapping time across space. *J. Vis.* **13**, 2–2 (2013).

31. Matthews, N. & Welch, L. Left visual field attentional advantage in judging simultaneity and temporal order. *J. Vis.* **15**, 7–7 (2015).

32. Zivi, P., Ferlazzo, F. & Sdoia, S. Perception of the temporal order of digits during rapid serial visual presentation is influenced by their ordinality. *Psychol. Res.* **87**, 1537–1548 (2023).

33. Zivony, A. & Eimer, M. The number of expected targets modulates access to working memory: A new unified account of lag-1 sparing and distractor intrusions. *J. Exp. Psychol. Hum. Percept. Perform.* **47**, 1543–1560 (2021).

34. Milton, A. & Pleydell-Pearce, C. W. The phase of pre-stimulus alpha oscillations influences the visual perception of stimulus timing. *NeuroImage* **133**, 53–61 (2016).

35. Vinck, M., Oostenveld, R., Van Wingerden, M., Battaglia, F. & Pennartz, C. M. A. An improved index of phase-synchronization for electrophysiological data in the presence of volume-conduction, noise and sample-size bias. *NeuroImage* **55**, 1548–1565 (2011).

36. Stam, C. J. & Van Straaten, E. C. W. Go with the flow: Use of a directed phase lag index (dPLI) to characterize patterns of phase relations in a large-scale model of brain dynamics. *NeuroImage* **62**, 1415–1428 (2012).

37. Callahan-Flintoft, C., Chen, H. & Wyble, B. A hierarchical model of visual processing simulates neural mechanisms underlying reflexive attention. *J. Exp. Psychol. Gen.* **147**, 1273–1294 (2018).

38. Tan, M. & Wyble, B. Understanding how visual attention locks on to a location: Toward a computational model of the N2pc component. *Psychophysiology* **52**, 199–213 (2015).

39. Hilkenmeier, F., Scharlau, I., Weiß, K. & Olivers, C. N. L. The dynamics of prior entry in serial visual processing. *Vis. Cogn.* **20**, 48–76 (2012).

40. Ronconi, L. & Melcher, D. The Role of Oscillatory Phase in Determining the Temporal Organization of Perception: Evidence from Sensory Entrainment. *J. Neurosci.* **37**, 10636–10644 (2017).

41. Davis, B., Christie, J. & Rorden, C. Temporal Order Judgments Activate Temporal Parietal Junction. *J. Neurosci.* **29**, 3182–3188 (2009).

42. Boenke, L. T., Zeghbib, A., Spiliopoulou, M., Alais, D. & Ohl, F. W. Prestimulus α/β power in temporal-order judgments: individuals differ in direction of

modulation but show consistency over auditory and visual tasks. *Front. Comput. Neurosci.* **17**, 1145267 (2023).

43. Richter, C. G., Coppola, R. & Bressler, S. L. Top-down beta oscillatory signaling conveys behavioral context in early visual cortex. *Sci. Rep.* **8**, 6991 (2018).

44. Otstavnov, N., Riaz, A., Moiseeva, V. & Fedele, T. Temporal and Spatial Information Elicit Different Power and Connectivity Profiles during Working Memory Maintenance. *J. Cogn. Neurosci.* **36**, 290–302 (2024).

45. Roberts, B. M., Hsieh, L.-T. & Ranganath, C. Oscillatory activity during maintenance of spatial and temporal information in working memory. *Neuropsychologia* **51**, 349–357 (2013).

46. Bonnefond, M. & Jensen, O. Alpha Oscillations Serve to Protect Working Memory Maintenance against Anticipated Distracters. *Curr. Biol.* **22**, 1969–1974 (2012).

47. Cravo, A. M., Rohenkohl, G., Wyart, V. & Nobre, A. C. Temporal Expectation Enhances Contrast Sensitivity by Phase Entrainment of Low-Frequency Oscillations in Visual Cortex. *J. Neurosci.* **33**, 4002–4010 (2013).

48. Yuan, P., Hu, R., Zhang, X., Wang, Y. & Jiang, Y. Cortical entrainment to hierarchical contextual rhythms recomposes dynamic attending in visual perception. *eLife* **10**, e65118 (2021).

49. Adhikari, B. M., Goshorn, E. S., Lamichhane, B. & Dhamala, M. Temporal-Order Judgment of Audiovisual Events Involves Network Activity Between Parietal and Prefrontal Cortices. *Brain Connect.* **3**, 536–545 (2013).

50. Moharramipour, A., Takahashi, T. & Kitazawa, S. Distinctive modes of cortical

communications in tactile temporal order judgment. *Cereb. Cortex* **33**, 2982–2996 (2023).

51. Battelli, L., Walsh, V., Pascual-Leone, A. & Cavanagh, P. The ‘when’ parietal pathway explored by lesion studies. *Curr. Opin. Neurobiol.* **18**, 120–126 (2008).

52. Nicholls, M. E. R. Hemispheric Asymmetries for Temporal Resolution: A Signal Detection Analysis of Threshold and Bias. *Q. J. Exp. Psychol. Sect. A* **47**, 291–310 (1994).

53. Verleger, R., Śmigasiewicz, K. & Möller, F. Mechanisms underlying the left visual-field advantage in the dual stream RSVP task: Evidence from N2pc, P3, and distractor-evoked VEPs. *Psychophysiology* **48**, 1096–1106 (2011).

54. Delorme, A. & Makeig, S. EEGLAB: an open source toolbox for analysis of single-trial EEG dynamics including independent component analysis. *J. Neurosci. Methods* **134**, 9–21 (2004).

55. De Cheveigné, A. ZapLine: A simple and effective method to remove power line artifacts. *NeuroImage* **207**, 116356 (2020).

56. Klug, M. & Kloosterman, N. A. Zapline-plus: A Zapline extension for automatic and adaptive removal of frequency-specific noise artifacts in M/EEG. *Hum. Brain Mapp.* **43**, 2743–2758 (2022).

57. Mullen, T. CleanLine EEGLAB plugin. *San Diego CA Neuroimaging Inform. Tools Resour. Clgh. NITRC* (2012).

58. Kothe, C., Miyakoshi, M. & Delorme, A. clean_rawdata. https://github.com/sccn/clean_rawdata (2019).

59. Pion-Tonachini, L., Kreutz-Delgado, K. & Makeig, S. ICLabel: An automated electroencephalographic independent component classifier, dataset, and website. *NeuroImage* **198**, 181–197 (2019).

60. Lopez-Calderon, J. & Luck, S. J. ERPLAB: an open-source toolbox for the analysis of event-related potentials. *Front. Hum. Neurosci.* **8**, 213 (2014).

61. Kappenman, E. S., Farrens, J. L., Zhang, W., Stewart, A. X. & Luck, S. J. ERP CORE: An open resource for human event-related potential research. *NeuroImage* **225**, 117465 (2021).

62. Miller, J., Patterson, T. & Ulrich, R. Jackknife-based method for measuring LRP onset latency differences. *Psychophysiology* **35**, 99–115 (1998).

63. Gramfort, A. *et al.* MEG and EEG data analysis with MNE-Python. *Front. Neurosci.* **7**, 267 (2013).

64. Fischl, B. FreeSurfer. *NeuroImage* **62**, 774–781 (2012).

65. Pascual-Marqui, R. D. Standardized low-resolution brain electromagnetic tomography (sLORETA): technical details. *Methods Find. Exp. Clin. Pharmacol.* **24 Suppl D**, 5–12 (2002).

66. Destrieux, C., Fischl, B., Dale, A. & Halgren, E. Automatic parcellation of human cortical gyri and sulci using standard anatomical nomenclature. *NeuroImage* **53**, 1–15 (2010).

67. Moca, V. V., Bârzan, H., Nagy-Dăbâcan, A. & Mureșan, R. C. Time-frequency super-resolution with superlets. *Nat. Commun.* **12**, 337 (2021).

68. Oostenveld, R., Fries, P., Maris, E. & Schoffelen, J.-M. FieldTrip: Open Source

Software for Advanced Analysis of MEG, EEG, and Invasive Electrophysiological Data. *Comput. Intell. Neurosci.* **2011**, 1–9 (2011).

69. Vinck, M., Van Wingerden, M., Womelsdorf, T., Fries, P. & Pennartz, C. M. A. The pairwise phase consistency: A bias-free measure of rhythmic neuronal synchronization. *NeuroImage* **51**, 112–122 (2010).

70. VanRullen, R. How to Evaluate Phase Differences between Trial Groups in Ongoing Electrophysiological Signals. *Front. Neurosci.* **10**, 426 (2016).

71. Voytek, B., D'Esposito, M., Crone, N. & Knight, R. T. A method for event-related phase/amplitude coupling. *NeuroImage* **64**, 416–424 (2013).

72. Bates, D., Mächler, M., Bolker, B. & Walker, S. Fitting Linear Mixed-Effects Models Using lme4. *J. Stat. Softw.* **67**, 1–48 (2015).

73. JASP Team. JASP (Version 0.95.4) [Computer software]. (2025).

74. Maris, E. & Oostenveld, R. Nonparametric statistical testing of EEG- and MEG-data. *J. Neurosci. Methods* **164**, 177–190 (2007).

Figure legends

Figure 1. Experimental paradigm and behavioral results.

(a) Schematic of a dual-target (TT) trial in the rapid serial visual presentation task. Participants monitored two lateral stimulus streams and reported one or two colored digit targets in their order of appearance while ignoring gray distractors. On TT trials, the first target (T1) was immediately followed by the second target (T2) at the same location and in the same color. **(b)** Examples of correct-order (CO) and order-reversal (OR) reports for the target pair shown in **a**. **(c)** OR rates for individual participants, expressed as the

percentage of all TT trials in which both target identities were correctly reported in reversed order. The dashed gray line indicates the probability of reporting the exact target pair in reversed order under uniform guessing of two distinct digits from eight alternatives: 1/(8 × 7) = 1.79%. **(d)** OR rates for targets presented in the left and right visual fields. Dots represent individual participants, and gray lines connect paired observations. The black line connects the group means, and error bars indicate ±1 standard error of the mean (SEM). * p = 0.023 for the two-sided paired-samples t test (t(26) = 2.41, d = 0.46, 95% CI [0.31, 3.91] percentage points). **(e)** Mean OR rates as a function of numerical distance between the targets (|T1 − T2|). The annotated coefficient and *p* value refer to the mean participant-level linear slope (*b* = −0.60, *p* = 0.010), with *b* expressed as the change in OR rate in percentage points per unit increase in numerical distance. Error bars indicate ±SEM. Data are from 27 participants.

Figure 2. ERP correlates of temporal-order reporting.

(a–c) Grand-average event-related potential waveforms for the N2pc **(a)**, P3b **(b)**, and occipital N400 (ON400; **c**) in TT trials with CO or OR reports, together with the CO–OR difference waveforms. Panel **a** shows contralateral-minus-ipsilateral activity at PO7/PO8; **b** shows activity averaged across P1, P2, and Pz; and **c** shows activity averaged across O1, O2, and Oz. Shaded regions indicate ±SEM. In **c**, thickened waveform segments and the purple horizontal bar mark the significant CO–OR temporal cluster spanning 392–476 ms after T1 onset, identified by cluster-based permutation testing. The inset scalp map shows the CO–OR amplitude difference averaged over this interval; gray stars denote electrodes belonging to the significant spatial cluster. **(d)** Descriptive participant-level summaries of ON400 mean amplitudes, averaged across O1, O2, and Oz within the interval identified in **c**. Dots represent individual participants, gray lines connect paired observations, and the black line connects the group means. Error bars indicate ±SEM. *** *p* < 0.001 for the paired comparison within this selected window. **(e)** Estimated cortical distribution of the CO–OR difference within the ON400 time window, obtained using standardized low-resolution brain electromagnetic tomography. The lateral view of the right hemisphere shows the significant cluster identified by source-space cluster-based permutation testing. Colors indicate *t* values for the CO–OR contrast. Time is relative to T1 onset; T2 appeared 100 ms later. Data are from 27 participants.

Figure 3. Oscillatory power associated with temporal-order reporting.

(a) Time–frequency map of the CO–OR power difference, expressed in decibels (dB) and averaged across the right posterior region of interest (ROI: CP4, CP6, TP8, P4, P6, P8, PO4, PO6, PO8, and O2). Black outlines indicate significant clusters identified by cluster-based permutation testing. Horizontal dashed lines indicate frequency-band boundaries. **(b)** Scalp distributions and descriptive participant-level summaries of early beta, late beta, and late theta–alpha power. Upper panels show the CO–OR power difference averaged over the corresponding time–frequency windows; stars denote electrodes belonging to significant spatial clusters. Lower panels show participant-level mean power extracted from the corresponding time–frequency windows and spatial electrode clusters. Dots represent individual participants, gray lines connect paired observations, and black lines connect the group means. Error bars indicate ±SEM. *** $p < 0.001$ for the paired comparisons within these selected windows and electrode sets. **(c)** Modulation of the relationship between single-trial power and OR probability by numerical distance. Curves show probabilities estimated from logistic generalized linear mixed-effects models, plotted against z-standardized single-trial power for early beta, late beta, and late theta–alpha activity. The Small, Medium, and Large curves are evaluated at numerical distances one standard deviation below the mean, at the mean, and one standard deviation above the mean, respectively. Annotated *b* coefficients and *p* values refer to the power × numerical distance interaction in each model. Shaded regions indicate 95% confidence intervals for the estimated probabilities. Time is relative to T1 onset; T2 appeared 100 ms later. Data are from 27 participants.

Figure 4. Phase-based analyses of temporal-order reporting.

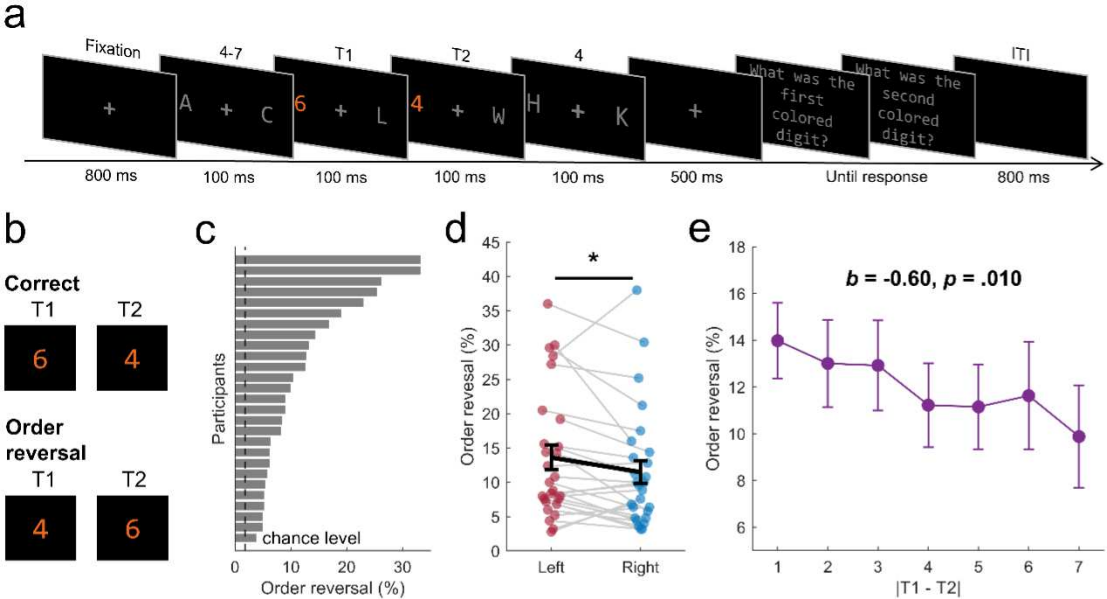
(a) Time–frequency map of the inter-trial phase coherence (ITPC) difference between CO and OR trials, averaged across all scalp electrodes. Trial counts were matched within each participant before ITPC estimation. The black outline indicates the significant cluster identified by cluster-based permutation testing. The inset scalp map shows the CO–OR ITPC difference averaged over the time–frequency window used for the follow-up spatial analysis; stars denote electrodes belonging to the significant spatial cluster. **(b)** Time–frequency map of the standardized phase-opposition sum, averaged across the parieto-occipital ROI (P1, Pz, P2, PO3, POz, PO4, PO5, PO6, PO7, PO8,

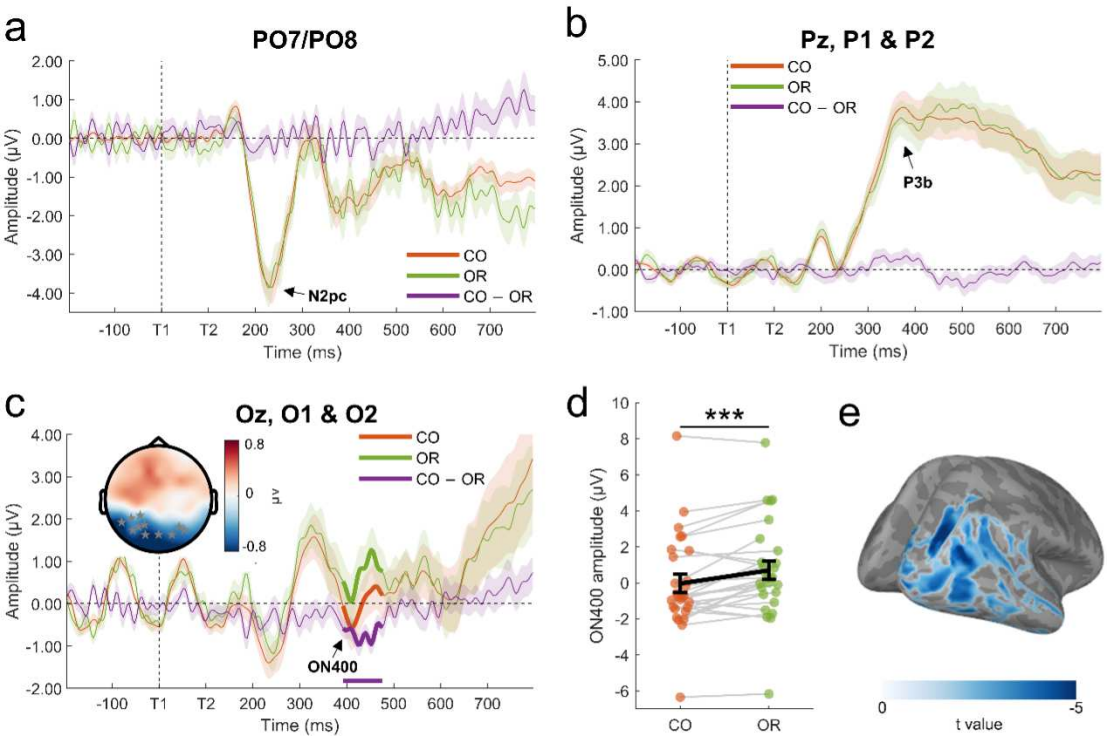
O1, Oz, and O2) and labeled zPOS in the color scale. This analysis assessed whether CO and OR trials were associated with distinct preferred oscillatory phases before T1 onset. The black curve marks the frequency-dependent exclusion boundary used to limit contamination from post-target activity due to wavelet temporal smearing. Only time–frequency points to the left of this curve were included in statistical testing. No significant clusters were identified in the analyzed pretarget region (all cluster-level *p* values > 0.271). **(c–d)** Time–frequency maps of the CO–OR difference in event-related phase–amplitude coupling, averaged across all scalp electrodes. The color scale (ΔerPAC) represents this between-condition difference. Coupling was computed between delta phase (1–4 Hz) and amplitude at 5–70 Hz in **c**, and between theta phase (4–7 Hz) and amplitude at 8–70 Hz in **d**. Neither analysis identified a significant CO–OR cluster (minimum cluster-level *p* = 0.507 for delta and 1.000 for theta). Horizontal dashed lines indicate frequency-band boundaries. Time is relative to T1 onset; T2 appeared 100 ms later. Data are from 27 participants.

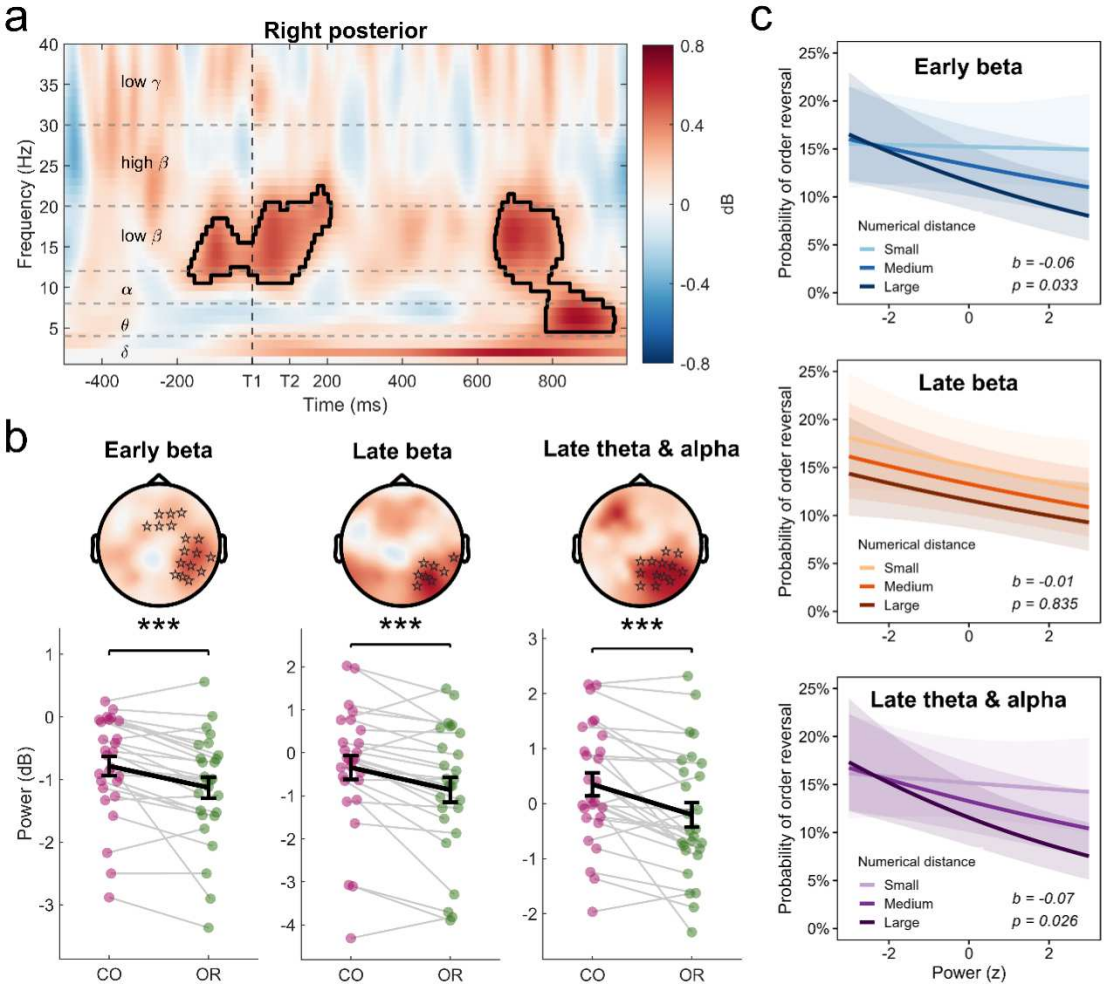
Figure 5. Late frontal–occipital synchronization and phase-leading asymmetry.

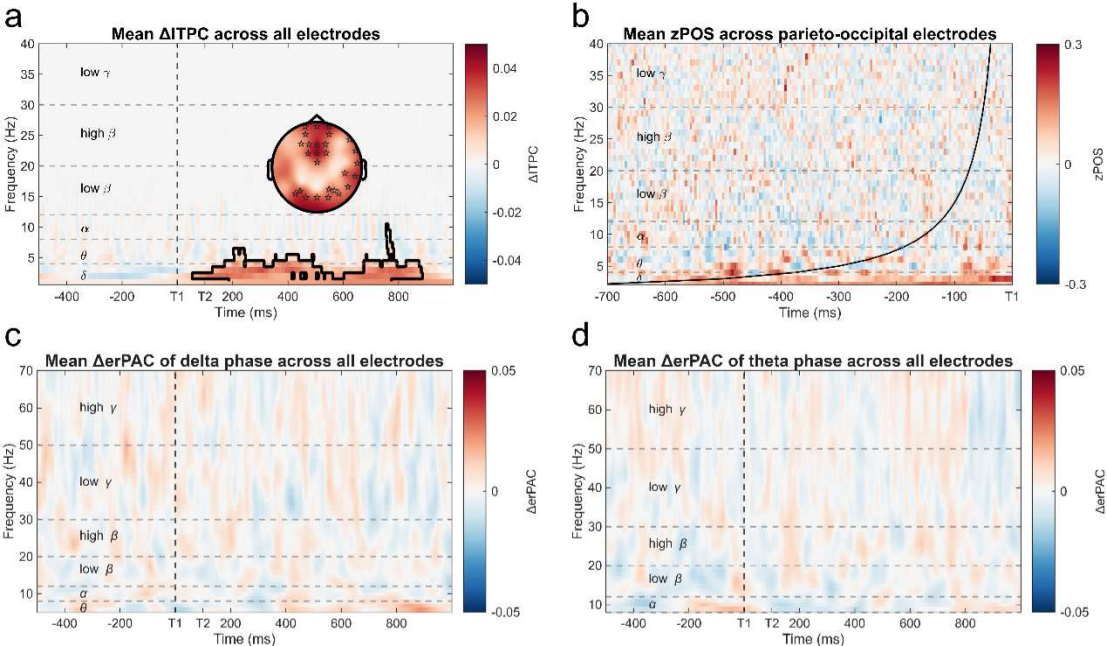
(a) Time–frequency map of the difference in the debiased squared weighted phase-lag index (dwPLI) between CO and OR trials for frontal–right-occipital electrode pairs. The color scale (ΔdwPLI) represents this between-condition difference. The black outline indicates the significant cluster spanning approximately 2–3 Hz and 530–860 ms after T1 onset, identified by cluster-based permutation testing. **(b)** Time courses of the directed phase-lag index (dPLI), averaged over 2–3 Hz, for CO and OR trials and for frontal–left-occipital and frontal–right-occipital electrode pairs. The LO and RO labels denote the left- and right-occipital electrode groups, respectively. Values above 0.5 indicate a frontal phase lead relative to the corresponding occipital electrode group, whereas values below 0.5 indicate an occipital phase lead. Shaded regions indicate ±SEM. Colored horizontal bars mark intervals in which dPLI differed significantly from 0.5 for the corresponding condition. The black horizontal bar marks the significant CO–OR difference for frontal–right-occipital electrode pairs. Significance was assessed using cluster-based permutation testing. To control for unequal trial counts, condition-specific dPLI estimates were averaged over 1,000 iterations of trial-count matching within

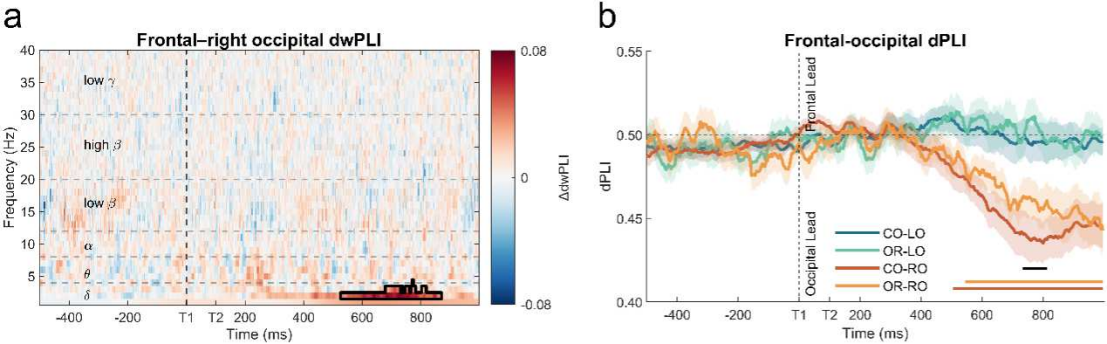
each participant. Time is relative to T1 onset; T2 appeared 100 ms later. Data are from 27 participants.


a
Fixation
4-7
T1
T2
4
ITI
What was the first colored digit?
What was the second colored digit?
800 ms
100 ms
100 ms
100 ms
100 ms
500 ms
Until response
800 ms
b
Correct
T1
T2
Order reversal
T1
T2
c
Participants
chance level
Order reversal (%)
d
Order revesal (%)
*
Left
Right
e
b = -0.60, p = .010
Order reversal (%)
|T1 - T2|


a
PO7/PO8
Amplitude (μV)
Time (ms)
N2pc
CO
OR
CO − OR
b
Pz, P1 & P2
P3b
c
Oz, O1 & O2
ON400
d
***
ON400 amplitude (μV)
e
t value


a
Right posterior
low γ
high β
low β
α
θ
δ
Frequency (Hz)
Time (ms)
T1
T2
dB
b
Early beta
Late beta
Late theta & alpha
***
Power (dB)
CO
OR
c
Probability of order reversal
Numerical distance
Small
Medium
Large
b = -0.06
p = 0.033
b = -0.01
p = 0.835
b = -0.07
p = 0.026
Power (z)


a
Mean ΔITPC across all electrodes
low γ
high β
low β
α
θ
δ
Frequency (Hz)
Time (ms)
ΔITPC
b
Mean zPOS across parieto-occipital electrodes
zPOS
c
Mean ΔerPAC of delta phase across all electrodes
high γ
low γ
high β
low β
ΔerPAC
d
Mean ΔerPAC of theta phase across all electrodes
T1
T2


a
Frontal–right occipital dwPLI
Frequency (Hz)
low γ
high β
low β
α
θ
δ
ΔdwPLI
0.08
0
-0.08
-400
-200
T1
T2
200
400
600
800
Time (ms)
b
Frontal-occipital dPLI
dPLI
0.55
0.50
0.45
0.40
Frontal Lead
Occipital Lead
CO-LO
OR-LO
CO-RO
OR-RO
Time (ms)